

Banner appropriate to article type will appear here in typeset article

Thermal fingers in cold channels: Thermo-viscous instability in dispersive flow

Federico Lanza¹, Gaute Linga^{1,2}, Fabian Barras¹, and Eirik G. Flekkøy^{1,3}

¹PoreLab, The Njord Centre, University of Oslo, Norway

²PoreLab, Department of Physics, Norwegian University of Science and Technology, Norway

³PoreLab, Department of Chemistry, Norwegian University of Science and Technology, Norway

Corresponding author: Federico Lanza, federico.lanza.5@gmail.com

(Received xx; revised xx; accepted xx)

An instability may occur when a hot viscous fluid, such as magma, flows into a thin gap and cools due to heat transfer to the surrounding environment, such as the host rock. Fluids that exhibit a drastic increase in viscosity as they cool give rise to a feedback loop where hotter regions flow faster, cooling more slowly, thus forming “fingers” of hot fluid. To investigate this phenomenon, we employ a model system in which hot fluid is injected into a Hele-Shaw cell where the confining plates exchange heat between the fluid and a cooler environment. We include both thermal diffusion and hydrodynamic dispersion in a two-dimensional description, allowing us to address the dependence of the instability on the Péclet number (ratio of advective to diffusive fluxes). We perform numerical simulations of temperature-dependent viscous fluid flow and find that finger-like instabilities emerge in response to small perturbations in the inlet velocity, depending on the Péclet number, the viscosity contrast between the hot injected fluid and the cooler displaced fluid, and the cooling rate through the plates. Using linear stability analysis, we compute the dispersion relation and determine how the fastest growth rate γ_{\max} and the corresponding wavenumber k_{\max} depend on these parameters. We also derive analytical expressions for γ_{\max} and k_{\max} valid in the regime of high Péclet number and high viscosity contrast. The results provide new insights into the mechanisms driving such instabilities, which could influence the formation and propagation of preferred pathways during fissure eruptions in geophysical contexts.

Key words: thermo-viscous fluid, dynamic instability, linear stability analysis, Hele-Shaw cell

1. Introduction

The flow of thermo-viscous fluids in confined geometries, such as fissures, porous media, or interfaces between contacting solids, is relevant to a variety of natural and industrial processes, such as subsurface magma flow, geothermal energy extraction (Mcdowell *et al.*

2016), enhanced oil recovery (Austin-Adigio & Gates 2020) as well as friction and lubrication between mechanical compounds (Bowden & Tabor 2001). In these systems, the fluid viscosity may depend strongly on temperature, typically decreasing as the temperature increases. This temperature-viscosity coupling introduces a feedback mechanism: A local increase in temperature reduces the viscosity, which in turn promotes faster flow in that region. As a result, small perturbations in the temperature or velocity field can become amplified, giving rise to the formation of finger-like structures and complex flow patterns.

A prominent example of thermo-viscous flow in a confined geometry is magma transport through the Earth's crust. The viscosity of magma can vary by several orders of magnitude in response to temperature changes of just a few hundred degrees Celsius (Blatt *et al.* 2006). Magma often flows through the Earth's crust via thin conduits, like fissures or dikes, whose thickness is much smaller than its other dimensions, effectively creating a quasi-planar geometry (Jones *et al.* 2017; Pansino *et al.* 2019). Natural manifestations include volcanic eruptions from linear fissure vents, such as the November 2023 eruption in Iceland (Sigmundsson *et al.* 2024), as well as sheet-like intrusions of magmatic rock, which often display finger-like structures (Galland *et al.* 2019). These regions of enhanced flow are typically referred to as channels or tubes, depending on their morphology and scale.

The prevalent interpretation of such finger patterns observed in the field is that they result from a Saffman–Taylor-type instability (Saffman & Taylor 1958; Homsy 1987), which occurs when a less viscous magma displaces a more viscous host rock (Pollard *et al.* 1975). The combined effects of viscosity contrast and geometrical confinement make this a natural setting for the development of viscous fingering, further modulated by temperature-dependent rheology.

A related class of instabilities arises in fluids with concentration-dependent viscosity (Tan & Homsy 1986, 1988; De Wit & Homsy 1999; Jha *et al.* 2011; De Wit 2020), where solute transport modifies the flow properties. In this case, the advection-diffusion equation for the solute concentration is formally analogous to that for temperature in thermo-viscous models, although key differences arise in the source terms, as thermal models typically include heat exchanges with boundaries, while solute transport may involve adsorption or reaction effects. These studies show that the non-linear coupling between concentration and viscosity can give rise to fingering instability dynamics analogous to those in thermo-viscous systems, with differences stemming from the specific transport mechanisms and boundary conditions.

Some experiments tried to reproduce finger instabilities in the laboratory adopting different fluids with significant thermal viscosity contrast, including paraffin wax (Whitehead & Helfrich 1991), corn syrup (Wylie *et al.* 1999), glycerin (Holloway & de Bruyn 2005; Nagatsu *et al.* 2009) and polyethylene glycol wax (Anderson *et al.* 2005). They showed that, for certain combinations of inlet flow rate and temperature contrast between the injected hot fluid and the cooler displaced fluid, small perturbations in the inlet flow can trigger a fingering instability. In particular Holloway & de Bruyn (2005) showed that the early stages of the instability obeys exponential growth and demonstrated the existence of a critical ratio between the viscosity of the hot injected fluid and the cooler displaced fluid below which instabilities may emerge.

Different numerical investigations have been conducted to characterize the conditions and properties of thermo-viscous instabilities in quasi-planar geometries (Helfrich 1995; Wylie & Lister 1995; Morris 1996; Wylie *et al.* 1999; Holloway & Bruyn 2006; Diniega *et al.* 2013). In this context, Helfrich (1995) studied thermo-viscous flow in a quasi-two-dimensional rectangular geometry using a gap-averaged model, combining linear stability analysis with numerical simulations. Assuming a high Péclet number (negligible thermal

diffusion), he showed that an instability may arise only if the viscosity ratio between hot and cold fluid is below a critical value. This threshold depends on the inlet condition, with values around $\approx 4.83 \cdot 10^{-2}$ for uniform pressure and $\approx 1.40 \cdot 10^{-3}$ for uniform transverse flow. Wylie & Lister (1995) performed simulations with a similar model to Helfrich (1995), combining it with linear stability analysis of a three-dimensional model. They demonstrated that the critical viscosity ratio is lower when considering three-dimensional perturbations compared to perturbations in the gap-averaged two-dimensional analogue. Other work focused on finding the most unstable perturbation wavelength and its dependence on system properties such as cell length (Morris 1996) or the cell gap width (Holloway & Bruyn 2006). However, all the numerical and theoretical studies mentioned, despite considering the limit of high Péclet number, did not account for hydrodynamic dispersion (Taylor 1953), which strongly influences scalar transport under the fluid shear that occurs for flows in narrow channels, especially at high Péclet numbers (Aris & Taylor 1956). This effect has been explicitly addressed in studies of miscible displacements involving concentration-dependent viscosity (Zimmerman & Homsy 1991, 1992; Ghesmat & Azaiez 2008; Pramanik & Mishra 2015; Keable *et al.* 2022), but remains largely unaccounted for in the literature on thermo-viscous Darcy flows.

In the present work, we provide new insights into the characterization of the fingering instability in thermo-viscous flow. We employ a gap-averaged model that accounts for both out-of-plane heat loss through thermal exchange with the confining plates and in-plane thermal dispersion. We perform time-dependent numerical simulations of the full nonlinear equations, investigating the development of the instability under both sinusoidal and random perturbations. We perform a linear stability analysis (LSA) of the model to numerically obtain the dispersion relation and identify the fastest growth rate γ_{\max} and its corresponding most-unstable wavenumber k_{\max} . Based on the linearized model, we obtain analytical scaling laws for how γ_{\max} and k_{\max} depend on key system parameters. By comparing the growth rate and wavenumber obtained from the LSA with those extracted from full simulations, we validate the capacity of the linear theory to capture the dominant features of the instability.

This article is organized as follows. In § 2, we introduce the governing equations and the base state solution. Section 3 presents results from time-dependent numerical simulations of the full nonlinear problem. The linear stability analysis is developed in § 4, where we also compare its predictions with the nonlinear simulation results. Finally, in § 5, we summarize and discuss the main findings.

2. Fully coupled gap-averaged model

We consider the injection of hot, less viscous fluid, into a planar geometry channel containing cold, more viscous fluid initially in equilibrium with the surroundings by heat transport through the confining walls. The model system is sketched in three dimensions in figure 1(a). Here, we seek to obtain an effective two-dimensional model, sketched in figure 1(b).

2.1. Model description and derivation

We assume that the flow is in the creeping regime (Feder *et al.* 2022), which means that the Reynolds number $Re = \rho U h / \mu \ll 1$, where ρ is the fluid density, U is a characteristic fluid velocity, h is the channel half-height, and μ is the dynamic viscosity of the fluid. The flow is then assumed to be governed by the Stokes equations, leading to the following mass

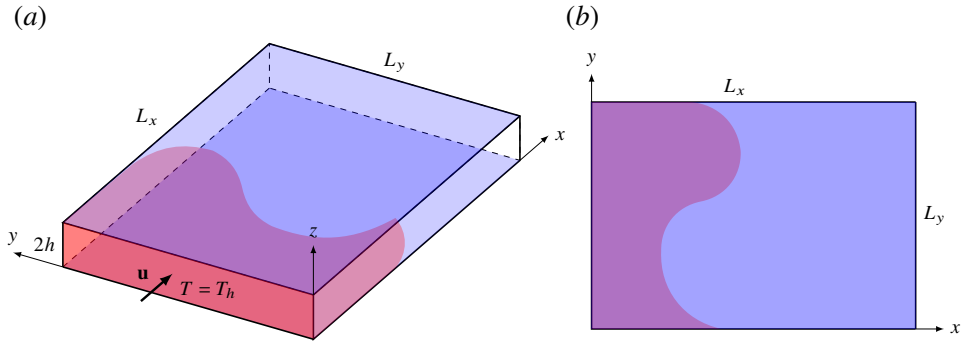


Figure 1. Schematic view of the model setup, with (a) a full three-dimensional view and (b) top view of the gap-averaged system considered in the present work. Hot, less viscous fluid, shown in red, is injected into a Hele-Shaw cell filled with colder, more viscous fluid. The cold, heat-conducting plates are shown in blue.

and momentum balance:

$$\nabla \cdot \mathbf{u} = 0, \quad (2.1)$$

$$\nabla \cdot [2\mu(T)\boldsymbol{\varepsilon}] = \nabla p. \quad (2.2)$$

Here, $\mathbf{u} = \mathbf{u}(x, y, z)$ is the velocity field, $p = p(x, y, z)$ the pressure field, the dynamic viscosity μ is a function of the temperature $T = T(x, y, z)$, while the symmetrized velocity gradient is given by $\boldsymbol{\varepsilon} = (\nabla\mathbf{u} + \nabla\mathbf{u}^\top)/2$. In this work, we use a first-order approximation of the Arrhenius model for the dynamic viscosity (Blatt *et al.* 2006), assuming an exponential dependence on temperature:

$$\ln \mu(T) = \frac{T_h - T}{T_h - T_c} \ln \mu_c + \frac{T - T_c}{T_h - T_c} \ln \mu_h, \quad (2.3)$$

where the subscripts c, h refer to the *cold* fluid initially in equilibrium with the plates, and the *hot* injected fluid, respectively. In equation (2.2) we also neglect buoyancy, that is, we assume that the Rayleigh number $Ra = \rho\delta gh^3(T_h - T_c)/(\kappa\mu_c) \ll 1$, where δ is the thermal expansion coefficient and g is the gravitational acceleration. This assumption implies that thermal convection is negligible compared to thermally induced viscosity-driven flow (Griffiths 1986).

The temperature T evolves in time through the thermal advection-diffusion equation,

$$\frac{\partial T}{\partial t} + \mathbf{u} \cdot \nabla T - \kappa \nabla^2 T = 0 \quad (2.4)$$

where the thermal diffusivity κ can be obtained from the fluid's heat conductivity α , specific heat capacity c and density ρ , as $\kappa = \alpha/(\rho c)$. In (2.4) we neglect viscous heating.

At the inlet, i.e. $x = 0$ as indicated in Figure 1(a), we impose that the hot fluid is injected according to a laminar flow profile at a constant flow rate, so the boundary conditions for the velocity and the temperature are given by

$$\mathbf{u}(x = 0) = \frac{3}{2}U \left(1 - \left(\frac{z}{h}\right)^2\right) \hat{\mathbf{e}}_x, \quad T(x = 0) = T_h, \quad (2.5)$$

where U is the imposed mean velocity, z is the out-of-plane coordinate, and $\hat{\mathbf{e}}_x$ is the unit vector in the x direction, i.e. the streamwise direction.

At the outlet, we impose a constant pressure and no thermal flux:

$$p(x = L) = p_0, \quad \hat{\mathbf{e}}_x \cdot \nabla T|_{x=L} = 0, \quad (2.6)$$

Thermal fingers in cold channels: Thermo-viscous instability in dispersive flow

At the plates, the boundary conditions are given by no-slip velocity and convective heat transfer between the channel and the surrounding environment:

$$\mathbf{u}(z = \pm h) = 0, \quad \hat{\mathbf{e}}_z \cdot \alpha \nabla T|_{\pm h} = H(T_c - T), \quad (2.7)$$

where H is the heat transfer coefficient, which in general depends on the thermal properties of both the fluid and the solid walls.

To find an effective 2D description of the system, we proceed by averaging the equations (2.1), (2.2) and (2.4) over the direction perpendicular to the plates, i.e. the z -direction. It is then natural to introduce the following gap-averaged quantities indicated by the subscript symbol \parallel :

$$p_{\parallel} = \frac{1}{2h} \int_{-h}^h p(x, y, z) dz, \quad \mathbf{u}_{\parallel} = \frac{1}{2h} \int_{-h}^h \mathbf{u}(x, y, z) dz, \quad T_{\parallel} = \frac{1}{2h} \int_{-h}^h T(x, y, z) dz. \quad (2.8)$$

The averaging of the governing equations is detailed in Appendix A. Here we briefly recall the key assumptions. First, we assume laminar flow, implying that the flow is always directed along the plane and follows a Poiseuille profile along the z -direction. Hence, it can be written as

$$\mathbf{u} = \frac{3}{2} \mathbf{u}_{\parallel} \left(1 - \left(\frac{z}{h} \right)^2 \right). \quad (2.9)$$

Moreover, we assume that the advection time along the streamwise extent of the domain, L_x/U (see figure 1), is much larger than the temperature diffusion time in the transverse direction, h^2/κ , i.e. that $L_x/U \gg h^2/\kappa$. The governing equations after gap-averaging are given by:

$$\nabla_{\parallel} \cdot \mathbf{u}_{\parallel} = 0 \quad (2.10)$$

$$-\frac{3}{h^2} \mu(T) \mathbf{u}_{\parallel} = \nabla_{\parallel} p_{\parallel} \quad (2.11)$$

$$\frac{\partial T_{\parallel}}{\partial t} + \mathbf{u}_{\parallel} \cdot \nabla_{\parallel} T_{\parallel} - \kappa \nabla_{\parallel}^2 T_{\parallel} - \frac{2}{105} \frac{h^2}{\kappa} \nabla_{\parallel} \cdot [\mathbf{u}_{\parallel} \otimes \mathbf{u}_{\parallel} \nabla_{\parallel} T_{\parallel}] + \frac{H}{h\rho c} (T_{\parallel} - T_c) = 0 \quad (2.12)$$

where $\nabla_{\parallel} = \hat{\mathbf{e}}_x \partial_x + \hat{\mathbf{e}}_y \partial_y$ is the gradient operator in the plane. To simplify the notation and isolate the key parameters influencing the model, we introduce the following non-dimensional variables:

$$\tilde{\mathbf{x}} = \frac{(x, y)}{h}, \quad \tilde{\mathbf{u}} = \frac{\mathbf{u}_{\parallel}}{U}, \quad \tilde{t} = \frac{U}{h} t, \quad \tilde{T} = \frac{T_{\parallel} - T_c}{T_h - T_c}, \quad \tilde{p} = \frac{h}{3\mu_c U} p_{\parallel} \quad (2.13)$$

We also define the viscosity ratio $\beta = \mu_h/\mu_c$, the rescaled cooling rate $\Gamma = H/(\rho c U)$ and the Péclet number $Pe = Uh/\kappa$. Leaving out all the tildes for brevity, Equations (2.10), (2.11) and (2.12) can be expressed in a dimensionless form as

$$\nabla \cdot \mathbf{u} = 0, \quad (2.14a)$$

$$\mathbf{u} = -\beta^{-T} \nabla p, \quad (2.14b)$$

$$\frac{\partial T}{\partial t} + \mathbf{u} \cdot \nabla T - \nabla \cdot [(\kappa \mathbf{I} + \kappa_{\parallel} \mathbf{u} \otimes \mathbf{u}) \nabla T] + \Gamma T = 0, \quad (2.14c)$$

where $\kappa = Pe^{-1}$ and $\kappa_{\parallel} = 2Pe/105$. The boundary conditions are

$$\mathbf{u}(x = 0) = \mathbf{e}_x, \quad T(x = 0) = 1, \quad \text{at the inlet}, \quad (2.15a)$$

$$\mathbf{p}(x = L_x) = 0, \quad \left. \frac{\partial T}{\partial x} \right|_{x=L_x} = 1 \quad \text{at the outlet}. \quad (2.15b)$$

The effective two-dimensional flow is governed by the Darcy law (2.14b), where the mobility increases with temperature. Equation (2.14c) is an advection-dispersion equation for the temperature field, with a local proportional loss term ΓT , representing the heat conducted through the confining plates, and an in-plane dispersion term which is the sum of two contributions. The first, proportional to κ , represents the isotropic thermal diffusion, while the second, proportional to κ_{\parallel} , results from hydrodynamic (Taylor) dispersion and enhances the effective diffusion only in the direction parallel to the velocity. The Péclet number controls both these contributions, as κ and κ_{\parallel} are directly and inversely proportional to Pe , respectively. In particular, thermal diffusion is important for $Pe \ll 1$, while for $Pe \gg 1$, Taylor dispersion dominates the in-plane heat transport. In both limits, dispersion is significant – hence, a model that includes only advection and neglects in-plane thermal diffusion cannot be consistently formulated.

The nonlinearly coupled partial differential equations (2.14) constitute the full gap-averaged model, in contrast to the linearized model discussed further in § 4.

2.2. Base state

To describe how the Péclet number, viscosity ratio, and heat conduction control the stability of the flow, we first characterize the *base state* of the model, which is what we denote the steady solution of the model (2.14) in the absence of any perturbations to the inlet condition (2.15a).

In the absence of any variations along the in-plane direction y parallel to the inlet, the model is effectively one-dimensional. The steady base state with a constant velocity along the x -direction is then given by

$$\mathbf{u}_0(x) = \hat{\mathbf{e}}_x, \quad T_0(x) = e^{-\xi x}, \quad p_0(x) = - \int_0^x \beta e^{\xi x'} dx' + C, \quad (2.16)$$

Here, C is a gauge constant that can be set to 0. We note in particular that the base-state temperature profile follows a negative exponential with characteristic length $1/\xi$, where

$$\xi = \frac{-1 + \sqrt{1 + 4\Gamma\kappa_{\text{eff}}}}{2\kappa_{\text{eff}}}. \quad (2.17)$$

where we define $\kappa_{\text{eff}} = \kappa + \kappa_{\parallel} = 1/Pe + 2Pe/105$.

3. Finger evolution using the full model

To investigate the response of the system to perturbations, we introduce deviations from the base state and examine how the flow evolves over time. A natural way to implement such perturbations is to modify the inlet boundary conditions (2.15). The governing equations (2.14) are then solved numerically in time, allowing us to track the spatial-temporal evolution of the temperature, pressure, and velocity fields. In what follows, we consider two types of perturbation: sinusoidal perturbations that consist of a single mode and random perturbations that consist of a spectrum of modes. The numerical finite element method used to solve the model in both cases is described in Appendix B.1.

Thermal fingers in cold channels: Thermo-viscous instability in dispersive flow

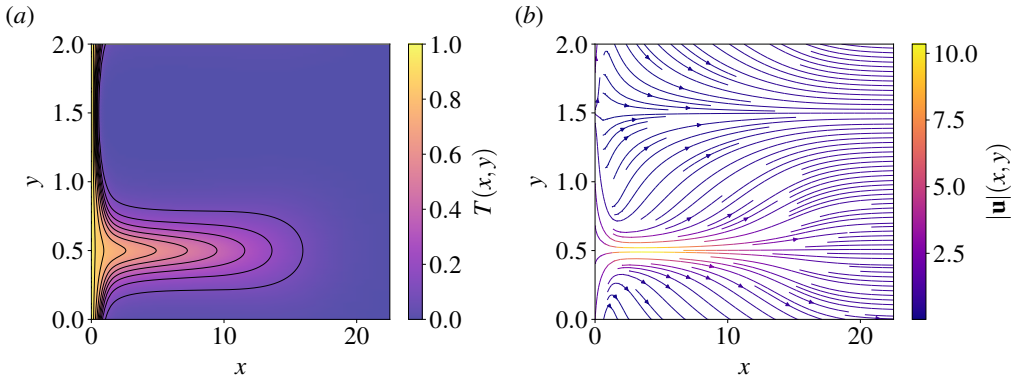


Figure 2. Instability emerging from a sinusoidal perturbation. (a) Temperature field $T(x, y)$ for $t = 20 \gg t_{\text{pert}}$, where different black contours represent different isothermal curves at $T = 0.1, 0.2, \dots, 0.9$. (b) Streamlines of the velocity field \mathbf{u} , where the local color represents the velocity magnitude $|\mathbf{u}|(x, y)$. For this simulation we set $Pe = 100$, $\Gamma = 1$, $\beta = 10^{-3}$ and $k = \pi$.

3.1. Sinusoidal perturbation

We first consider instabilities arising from a sinusoidal perturbation of the base state. We prepare the system in the base state (2.16) at time $t = 0$, and then change the inlet velocity boundary condition for a small time interval $t \in (0, t_{\text{pert}}]$. The sinusoidal perturbation in the velocity field can then be written as follows:

$$u_x(0, y, t) = \begin{cases} 1 + \epsilon \sin(ky) & \text{for } t \leq t_{\text{pert}} \\ 1 & \text{for } t > t_{\text{pert}}, \end{cases} \quad (3.1)$$

where ϵ is the perturbation amplitude and k is its wavenumber. For all simulations shown here, we set $\epsilon = 10^{-3} \ll 1$ and $t_{\text{pert}} = 0.1$. Different simulations are then fully characterized by a specific combination of Pe , Γ , β and k .

To reduce the influence of lateral boundaries, we apply periodic boundary conditions at the transverse sides of the domain, i.e., at $y = 0$ and $y = L_y$ (see figure 1). For a given value of k , the transverse system size is set to $L_y = 2\pi/k$, ensuring that the perturbation spans exactly one wavelength.

To see if an instability arises, we observe the behavior of the system at times sufficiently larger than t_{pert} . For different combinations of the global parameters and the wavenumber, an instability emerges and leads to the formation of a *thermal finger*. The system progressively moves away from the base state until it reaches a stationary state for $t \gg t_{\text{pert}}$.

An example is shown in figure 2, where the temperature and velocity profiles of a system in such a state are shown. In particular, the temperature field $T(x, y)$ is shown in figure 2(a). The deviation from an exponential profile uniform along y is clearly visible, with a high-temperature region arising close to the inlet at the position of the maximum of the perturbation ($y = 0.5$ in the figure), whose contours, emphasized by the isothermal curves, resemble a finger shape. The effects of the instability are also visible by looking at the velocity streamlines in figure 2(b), where the flow that is focused in correspondence to the finger region strongly deviates from a uniform flow profile. Far from the inlet, for x sufficiently high, the effects of the perturbation vanish and the temperature and velocity field become uniform.

To quantify the onset and growth of an instability, an effective way is to consider the difference between the maximum and minimum of a relevant physical quantity. With this aim, we measure the span between the maximum and minimum of both the temperature

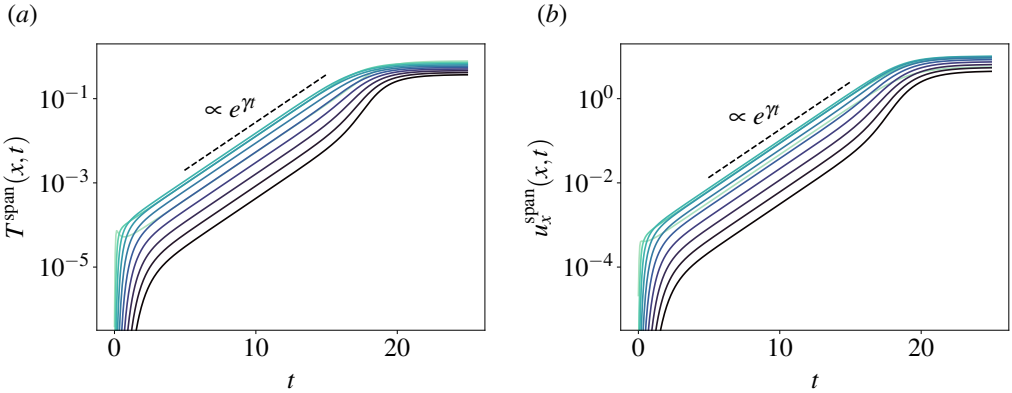


Figure 3. Temporal evolution of the spans in (a) temperature, $T^{\text{span}}(x, t)$ (see (3.2a)), and (b) streamwise velocity, $u_x^{\text{span}}(x, t)$ (see (3.2b)), for a sinusoidal inlet velocity perturbation. Different positions x are represented using a color gradient ranging from light blue ($x = 1$) to dark blue ($x = 10$), with values equally spaced by 1. The dashed line indicates the slope of the curves obtained by a best fit procedure in the corresponding time interval. The simulation corresponds to figure 2 with $Pe = 100$, $\Gamma = 1$, $\beta = 10^{-3}$ and $k = \pi$.

field and the x -component of the velocity field, denoted T^{span} and u_x^{span} , respectively:

$$T^{\text{span}}(x, t) = T^{\text{max}}(x, t) - T^{\text{min}}(x, t), \quad (3.2a)$$

$$u_x^{\text{span}}(x, t) = u_x^{\text{max}}(x, t) - u_x^{\text{min}}(x, t). \quad (3.2b)$$

Here, the superscripts max and min refer, respectively, to the maximum and minimum value of the related quantity along y , given x and t . For the sinusoidal perturbations considered in this subsection, we expect the maximum and minimum to occur at $y = \pi/(2k)$ and $y = 3\pi/(2k)$, respectively, for all x and t .

Initially and as long as the relative amplitude of the perturbation remains small, we expect the instability to evolve exponentially in time, i.e. like

$$T^{\text{span}}(x, t) \propto e^{\gamma t}, \quad u_x^{\text{span}}(x, t) \propto e^{\gamma t} \quad (3.3)$$

where γ is the growth rate of the instability. If $\gamma < 0$, the perturbation decays, meaning that the base state is stable, while if $\gamma > 0$ the system is unstable and the exponential behavior holds as long as non-linear growth-limiting effects remain negligible.

Figure 3 shows the temporal evolution of both the temperature and velocity spans for an unstable system. We see that, after a short transient phase, both quantities grow exponentially in time, corresponding to the linear growth phase, until they slow down and eventually saturate at a plateau corresponding to a stationary state distinct from the base state.

The exponential behavior is robust for different choices of x sufficiently close to the inlet. From a linear fit of the couples $(\log T^{\text{span}}, t)$ (or $(\log u_x^{\text{span}}, t)$), in a time interval corresponding to the linear phase, it is then possible to measure the growth rate γ .

3.2. Random perturbation

In real physical systems, perturbations are rarely limited to a single mode, but rather consist of a superposition of several modes, often with random phases and amplitudes. To mimic natural perturbations, we now consider a white-noise perturbation in which all spatial modes are present with equal amplitude but random phase. This initial condition allows all

Thermal fingers in cold channels: Thermo-viscous instability in dispersive flow

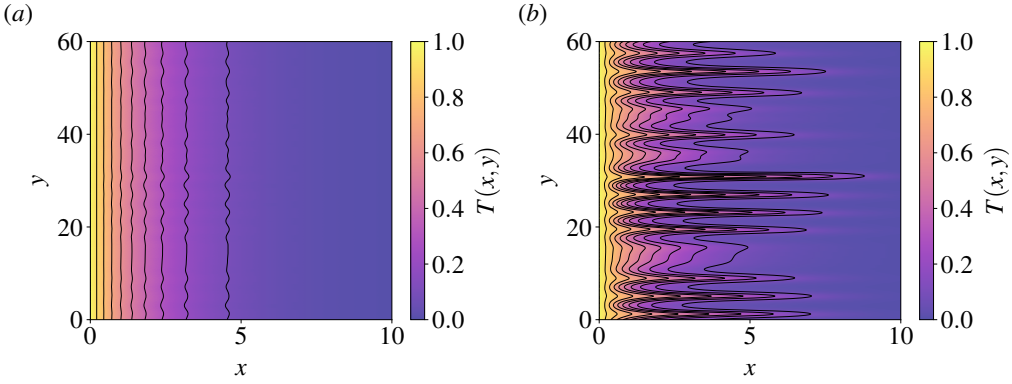


Figure 4. Instability emerging from a random perturbation. The temperature field $T(x, y, t)$ is shown at two time instances (a) $t = 5$ and (b) $t = 9$. The black contours represent different isothermal curves at $T = 0.1, 0.2, \dots, 0.9$. (b). For this simulation we set $Pe = 100$, $\Gamma = 1$, and $\beta = 10^{-3}$.

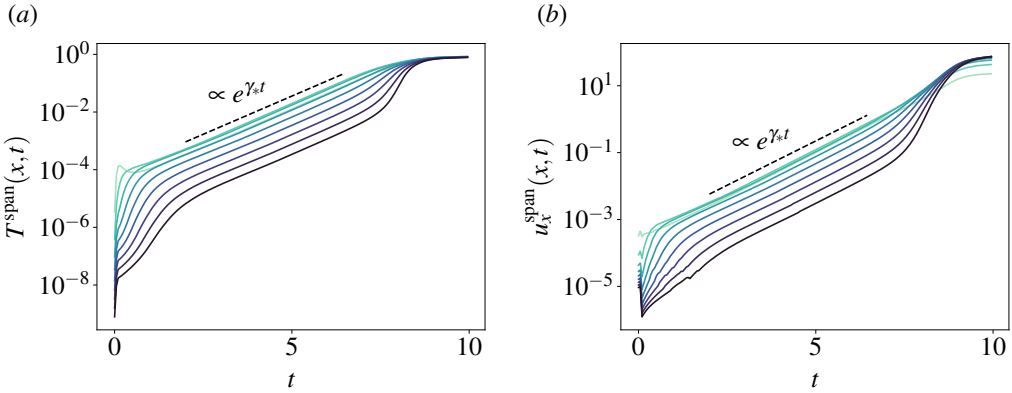


Figure 5. Temporal evolution of the span in (a) temperature, $T^{\text{span}}(x, t)$ (see (3.2a)), and (b) streamwise velocity, $u_x^{\text{span}}(x, t)$ (see (3.2b)), for a random inlet velocity perturbation. Different positions x are represented using a color gradient ranging from light blue ($x = 1$) to dark blue ($x = 10$), with values equally spaced by 1. The dashed line indicates the slope of the curves obtained by a best fit procedure in the corresponding time interval. The simulation corresponds to figure 4, with $Pe = 100$, $\Gamma = 1$, and $\beta = 10^{-3}$.

modes to evolve simultaneously, with the unstable ones growing and eventually dominating the behavior of the system.

We implement a white-noise perturbation by the following boundary condition for the velocity at the inlet:

$$u_x(0, y, t) = \begin{cases} 1 + \epsilon\eta(y) & \text{for } t \leq t_{\text{pert}} \\ 1 & \text{for } t > t_{\text{pert}} \end{cases} \quad (3.4)$$

where $\eta(y)$ is an uncorrelated random variable distributed according to a Gaussian distribution centered at $\langle \eta \rangle = 0$ and with a variance $\langle \eta^2 \rangle = 1$. Like in the previous subsection, we implement periodic boundary conditions at $y = 0$ and $y = L_y$, although in this case the transverse system size is not related to any specific perturbation wavelength.

Figure 4 shows the development of the instability triggered by an initial random perturbation, in a single simulation with parameters $Pe = 100$, $\Gamma = 1$, and $\beta = 10^{-3}$. The panels (a) and (b) show the temperature field $T(x, y)$ at times $t = 5$ and $t = 9$, both

significantly larger than the perturbation time $t_{\text{pert}} = 0.1$. The evolving distortion of the temperature field is emphasized by the isothermal curves.

In panel (a), corresponding to the linear growth regime, only a subset of modes is visibly amplified, reflecting the selective growth of wavelengths predicted by linear theory. This selection becomes even clearer in panel (b), which represents a later time when nonlinear effects have become significant: The amplitude of the most unstable mode has increased substantially, and its structure dominates the pattern. The dominant wavelength k_* is estimated from the number of emerging fingers n_f visible in the interval $0 < y < L_y$, using the relation $k_* = 2\pi n_f / L_y$.

To quantify the growth of the instability, we track the evolution of the spans $T^{\text{span}}(x, t)$ and $u_x^{\text{span}}(x, t)$, defined in equation (3.2). Figure 5 displays their time evolution for various locations along x . Analogously to the sinusoidal perturbation case, a period of exponential growth is evident, indicated by the dotted reference line, between an initial transient period and a final non-linear regime. We find that during the linear growth phase both quantities scale as $e^{\gamma_* t}$, where γ_* denotes the growth rate of the fastest mode.

The late-stage stabilization of fingers to steady, finite-length structures reflects the balance between the temperature advection inside the cell and the cooling through the walls, and has been addressed in previous numerical studies (Helfrich 1995; Diniega *et al.* 2013). In this paper, we focus on the early stage of the instability and on the physics that controls its emergence in thermo-viscous flow, leaving the characterization of the long-time steady state a topic for further study.

4. Linear stability analysis

To gain insight into the mechanisms underlying the instability observed in the simulations of the full model, we now turn to a linear stability analysis of the governing equations. By considering small perturbations around the base state, the equation system can be linearized, allowing us to examine the growth rates and structure of individual modes in the early, exponential phase of the instability. This approach yields a dispersion relation, from which the maximum growth rate and its associated most unstable wavenumber can be determined.

4.1. Derivation

To derive the linearized problem from the full model (2.14), we follow a standard procedure (see e.g. (Helfrich 1995)). We introduce a perturbation around the base state, such that a solution can be written as

$$p(x) = p_0(x) + p'(x, y, t) \quad (4.1a)$$

$$T(x) = T_0(x) + T'(x, y, t) \quad (4.1b)$$

$$\mathbf{u}(x) = \mathbf{u}_0(x) + \mathbf{u}'(x, y, t) \quad (4.1c)$$

where T' , $\mathbf{u}' = (u'_x, u'_y)$ and p' are the perturbation terms for the temperature, velocity, and pressure, respectively, and we have $T' \propto \epsilon$, $|\mathbf{u}'| \propto \epsilon$ and $p' \propto \epsilon$, where $\epsilon \ll 1$ is a small perturbation parameter related to the deviation from the base state at the inlet; see equations (3.1) and (3.4). Keeping only terms of first order in ϵ , equations (2.14a), (2.14b), (2.14c) become:

$$\partial_x^2 u'_x - \psi \partial_x T_0 \partial_x u'_x + \partial_y^2 u'_x = \psi \partial_y^2 T' \quad (4.2a)$$

$$\partial_t T' + u'_x \partial_x T_0 + \partial_x T' - \kappa^2 \nabla^2 T' - \kappa_{\parallel} (\partial_x^2 T' + \partial_x u'_x \partial_x T_0 + 2u'_x \partial_x^2 T_0) = -\Gamma T' \quad (4.2b)$$

Thermal fingers in cold channels: Thermo-viscous instability in dispersive flow

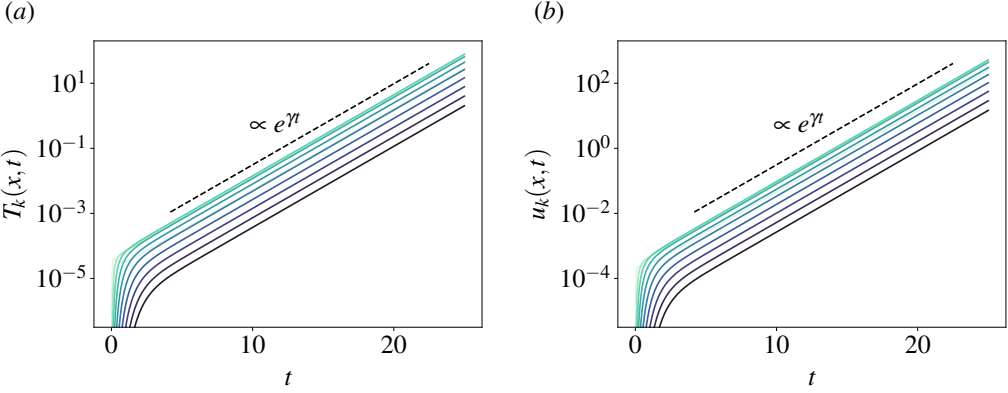


Figure 6. Temporal evolution of the Fourier-transformed perturbation term for (a) the temperature T_k and (b) the streamwise velocity u_k . Different positions x are represented using a color gradient ranging from light blue ($x = 1$) to dark blue ($x = 10$), with values equally spaced by 1. The dashed line indicates the slope of the curves obtained by a best fit procedure in the corresponding time interval, from which we measured $\gamma = 0.57392 \pm 10^{-5}$. Here the simulation parameters are $Pe = 100$, $\Gamma = 1$, $\beta = 10^{-3}$, and $k = \pi$.

Here we have defined $\psi = -\log \beta > 0$ for brevity. Equation (4.2a) is obtained by combining the incompressibility condition $\nabla \cdot \mathbf{u}' = 0$ with the perturbed Darcy law, expressing the perturbed velocity as a function of the pressure and temperature perturbation terms:

$$\mathbf{u}' = -\beta^{-T_0} \nabla p' + \psi T' \hat{\mathbf{x}}. \quad (4.3)$$

Equation (4.2b) is obtained keeping the linear terms of the advection-diffusion equation (2.14c). Note that both (4.2a) and (4.2b) present only two perturbation fields, namely T' and u'_x . A linear instability can then be identified by finding a solution for these two fields. The boundary conditions for (4.2) are

$$T'(0, y, t) = T'(\infty, y, t) = T'(x, y, 0) = 0, \quad \text{and} \quad u'_x(0, y, t) = \epsilon e^{iky}. \quad (4.4)$$

We now take the Fourier transform in the y direction, i.e. express

$$T'(x, y, t) = T_k(x, t) e^{iky}, \quad u'_x(x, y, t) = u_k(x, t) e^{iky}, \quad (4.5)$$

which inserted into (4.2) gives an equation system for T_k and u_k :

$$\partial_x^2 u_k - \psi \partial_x T_0 \partial_x u_k - k^2 u_k = -k^2 \psi T_k \quad (4.6a)$$

$$\partial_t T_k + \partial_x T_k - \kappa_{\text{eff}} \partial_x^2 T_k + [\kappa k^2 + \Gamma] T_k = \partial_x T_0 (-u_k + \kappa_{\parallel} \partial_x u_k) + 2\kappa_{\parallel} u_k \partial_x^2 T_0 \quad (4.6b)$$

with the boundary conditions

$$T_k(0, t) = T_k(\infty, t) = T_k(x, 0) = 0, \quad (4.7a)$$

$$u_k(0, y, t) = \epsilon. \quad (4.7b)$$

The problem (4.6)-(4.7) is solved numerically using a finite element method (see Appendix B.2).

The solutions for $T_k(x, t)$ and $u_k(x, t)$ are shown as functions of time t for different streamwise positions x in figure 6, where we have set $Pe = 100$, $\Gamma = 1$ and $\beta = 10^{-3}$. After an initial transient interval, both functions follow a steady exponential growth in time. The slope of each curve does not depend on the choice of x , indicating that the whole function approaches a constant spatial shape and only its scale evolves in time. For a given set of parameters, the growth rate $\gamma = \gamma(k)$ related to the spatial frequency k of the perturbation

is then measured by a least-squares linear fit to this perturbation scale. For a robust and unbiased measure of the perturbation scale, we use the maximum value of T_k along x , i.e. $T_{\max}(t) = \max_x T_k(x, t)$.

Assuming a time-invariant shape and exponential growth of the perturbation is equivalent to writing:

$$T_k(x, t) = \hat{T}_k(x)e^{\gamma t}, \quad u_k = \hat{u}_k(x)e^{\gamma t}. \quad (4.8)$$

Inserting (4.8) into equations (4.6) leads to a system of ordinary differential equations (ODE) for $\hat{T}_k(x)$ and $\hat{u}_k(x)$:

$$\left(\frac{d^2}{dx^2} - \psi \frac{dT_0}{dx} \frac{d}{dx} - k^2 \right) \hat{u}_k = -k^2 \psi \hat{T}_k, \quad (4.9a)$$

$$\left(\gamma + \frac{d}{dx} - \kappa_{\text{eff}} \frac{d^2}{dx^2} + \kappa k^2 + \Gamma \right) \hat{T}_k = \left(-\frac{dT_0}{dx} + \kappa_{\parallel} \left(2 \frac{d^2 T_0}{dx^2} + \frac{dT_0}{dx} \frac{d}{dx} \right) \right) \hat{u}_k. \quad (4.9b)$$

The system (4.9) is generally not solvable analytically. However, in the outer region ($x \gg \xi^{-1}$) we can set $T_0 = 0$, so equations (4.9a) and (4.9b) are simplified as, respectively,

$$\left(\frac{d^2}{dx^2} - k^2 \right) \hat{u}_k = -k^2 \psi \hat{T}_k, \quad (4.10a)$$

$$\left(\gamma + \frac{d}{dx} - \kappa_{\text{eff}} \frac{d^2}{dx^2} + \kappa k^2 + \Gamma \right) \hat{T}_k = 0. \quad (4.10b)$$

Applying the boundary condition $\hat{T}_k(x \rightarrow \infty) = 0$, the solution can be written as

$$\hat{T}_k(x) = A e^{-\Lambda x}, \quad (4.11a)$$

$$\hat{u}_k(x) = \frac{\psi k^2}{k^2 - \Lambda^2} A e^{-\Lambda x} + B e^{-kx}, \quad (4.11b)$$

where A and B are undefined constants and

$$\Lambda = \frac{-1 + \sqrt{1 + 4(\Gamma + \kappa k^2 + \gamma)\kappa_{\text{eff}}}}{2\kappa_{\text{eff}}} \quad (4.12)$$

is the inverse of the exponential decay length.

In figure 7, we show the evolution along x of the rescaled perturbation terms $T_k(x, t)/T_{\max}(t)$ and $u_k(x, t)/u_{\max}(t)$, where $T_{\max}(t) = \max_x T_k(x, t)$ and $u_{\max}(t) = \max_x u_k(x, t)$. Both functions increase sharply for small values of x , followed by a monotonic decrease that is exponential for large x . In particular, the slope of the exponential tail for the temperature term T_k matches, for sufficiently high t , the one from the analytical solution (4.11a) valid for $x \gg \xi^{-1}$.

4.2. Dispersion relations

For any combination of viscosity ratio β , cooling rate Γ , Péclet number Pe , and wavenumber k of the perturbation, it is possible to numerically measure the growth rate γ and thereby establish a dispersion relation $\gamma(k; Pe, \Gamma, \beta)$.

Figure 8 shows an intensity map of the growth rate γ as a function of β , Γ , and Pe in panels (a-c), respectively. For each plotted parameter, the other two are kept constant and fixed to the values shown below. For a given combination of Pe , Γ and β , the dispersion relation $\gamma(k)$ corresponds to a vertical section of the intensity map based on these values.

The plots in figure 8 reveal a non-trivial dependence of the growth rate on the wavenumber and the three global parameters. For each parameter, the shape of the contours, representing

Thermal fingers in cold channels: Thermo-viscous instability in dispersive flow

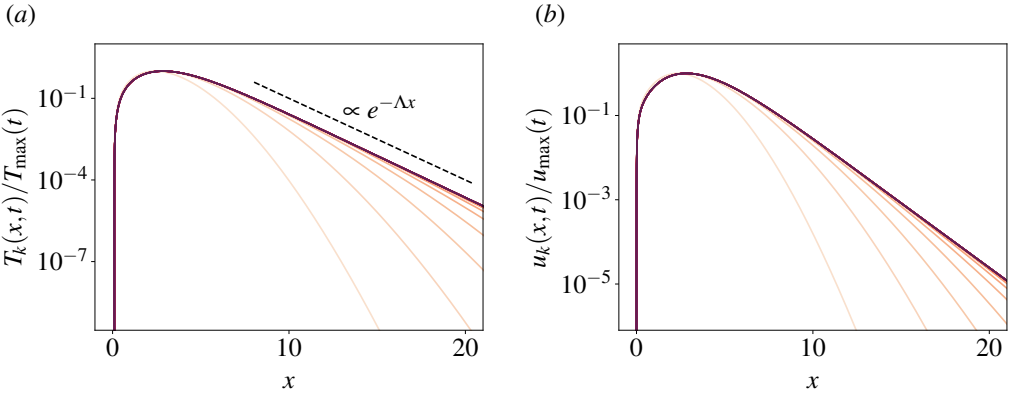


Figure 7. Fourier-transformed perturbation term for (a) the temperature T_k and (b) the streamwise the velocity u_k , as a function of the position x . Different times t are represented using a color gradient ranging from light red ($t = 1$) to dark red ($t = 10$), with values equally spaced by 1. The dashed line in (a) represents the slope of the exponential solution (4.11a) with $\Lambda = 0.69102 \pm 10^{-5}$. The simulation corresponds to figure 6 with $Pe = 100$, $\Gamma = 1$, $\beta = 10^{-3}$, and $k = \pi$.

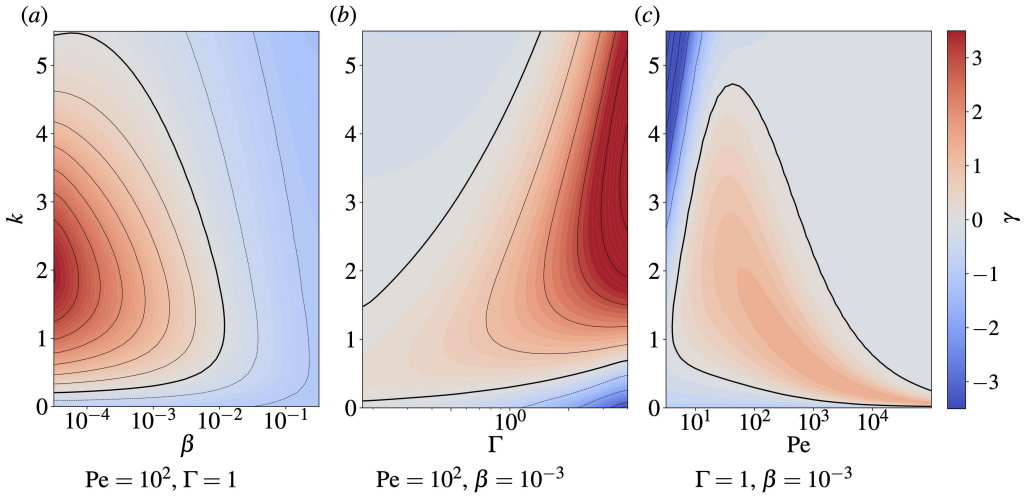


Figure 8. Parameter space of the instability growth rate γ as a function of the wavenumber k and the system parameters Pe , Γ and β . Each panel shows $\gamma(k; Pe, \Gamma, \beta)$ for different values of one parameter while keeping the other two fixed: (a) viscosity ratio β , (b) cooling rate Γ , (c) Péclet number Pe . The color represents the magnitude of γ , with red regions indicating higher growth rates and blue regions indicating stable regimes. The thicker black contour line marks the $\gamma = 0$ boundary, separating stable and unstable regions in the parameter space.

points with the same value of γ , depends strongly on the values of the other two parameters that are held fixed. Before we present a prediction for the peak locations in the next subsection, we can make a few preliminary observations.

First, for some combinations of Pe , Γ and β , $\gamma(k) < 0$ for all k , while for other choices of these global parameters, there exists an interval of values of k for which $\gamma(k) > 0$. The instability grows only for perturbation wavelengths whose corresponding growth rate is positive. This implies that for combinations of Pe , Γ and β for which γ is always negative, an instability cannot develop from any kind of perturbation, and the system is unconditionally stable. On the other hand, if an interval of positive γ exists, an instability is expected to

grow only under perturbations that contain modes of the corresponding wavenumber k . In general, the interval of positive γ changes with the combination of Pe , Γ and β .

Second, for all the explored combinations of parameters, cross sections of γ along k exhibit exactly one global maximum. We denote this maximum growth rate $\gamma_{\max} = \max_k \gamma(k)$, and its corresponding wavenumber k_{\max} , that is the value of k for which $\gamma(k_{\max}) = \gamma_{\max}$. For a perturbation composed of a spectrum of wavenumbers, we expect the instability to grow at the wavenumber corresponding to the fastest growth rate in the spectrum, at least until non-linear terms start to be relevant. In particular, if the perturbation consists of white noise, as discussed in § 3.2, an instability will develop at a wavelength equal to $2\pi/k_{\max}$ and will grow exponentially at a rate equal to γ_{\max} , at least at times sufficiently small for the linear stability approximation to hold. This growth requires that $\gamma_{\max} > 0$; otherwise it will decay. To predict the evolution of instabilities under such conditions, we need to study how k_{\max} and γ_{\max} depend on the global parameters.

4.3. Evolution of the maximum growth rate and corresponding wavenumber

In the general case, we expect that the maximal growth rate γ_{\max} and the most unstable wavenumber k_{\max} reflect some of the complexity of the dispersion relation described in the previous subsection. However, in the limit of high Péclet number, $Pe \gg 1$, we find the analytical predictions (see Appendix C):

$$\gamma_{\max}(Pe, \Gamma, \beta) \simeq \Gamma \tilde{\gamma}_{\max}(\beta), \quad (4.13a)$$

$$k_{\max}(Pe, \Gamma, \beta) \simeq \sqrt{\frac{\Gamma}{Pe}} \tilde{k}_{\max}(\beta), \quad (4.13b)$$

where $\tilde{\gamma}_{\max}$, \tilde{k}_{\max} are dimensionless functions of the viscosity ratio alone. For a given β , γ_{\max} is expected to reach a constant value proportional to Γ for large Pe , while k_{\max} is expected to scale like $\Gamma^{1/2} Pe^{-1/2}$. These new scaling laws can be directly tested against numerical data in the following.

In the additional limit of low viscosity ratio, $\beta \ll 1$, we find approximately

$$\tilde{\gamma}_{\max}(\log \beta) \simeq a_2 \log^2 \beta + a_1 \log \beta + a_0, \quad (4.14a)$$

$$\tilde{k}_{\max}(\log \beta) \simeq b_1 \log \beta + b_0, \quad (4.14b)$$

where a_0 , a_1 , a_2 , b_0 and b_1 are numerical constants (approximate values are given in table 1). For sufficiently large Pe , we find these polynomial expressions to yield good agreement with numerical data for all unstable configurations, as we will show in the following. The derivation of (4.13) and (4.14) is based on scaling equations (4.9), neglecting small terms, and grouping the independent parameters, as detailed in Appendix C.

We numerically compute how the fastest growth rate and the corresponding wavenumber depends on the global parameters and eventually compare it with (4.14). To find γ_{\max} and k_{\max} for a given combination of global parameters Pe , Γ , and β , we compute γ by solving (4.6) and (4.7) for an interval of values of k that includes the maximum and locate the maximum using a quadratic fit to these values. The coordinate of the maximum from the best fit corresponds to $(k_{\max}, \gamma_{\max})$. Next, we discuss how the stability of thermo-viscous flow evolves with the three control parameters β , Γ and Pe .

In figure 9, 10 and 11 we plot γ_{\max} (panels (a) and (c)) and k_{\max} (panels (b) and (d)) as functions of β , Γ and Pe , respectively. For each plotted parameter, the other two are kept constant to a selected combination of values specified in the figures caption and legend. For all three figures, the comparison with the prediction from equations (4.14) is shown

Thermal fingers in cold channels: Thermo-viscous instability in dispersive flow

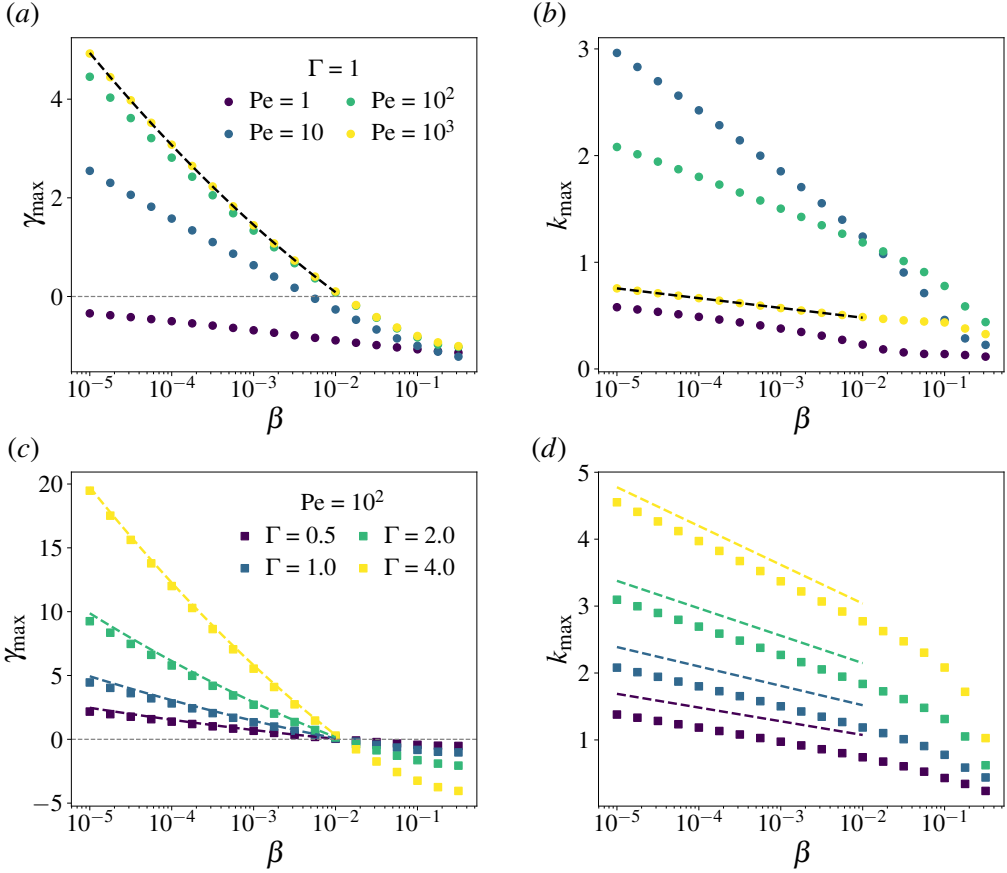


Figure 9. Maximum growth rate γ_{\max} ((a) and (c)) and corresponding wavenumber k_{\max} ((b) and (d)) as functions of the viscosity ratio $\beta \in [10^{-5}, 10^{-0.5}]$. (a) and (b) show the dependence on β for various Pe at fixed $\Gamma = 1$. The black dashed line in (a) shows the fit of the $Pe = 10^3$ data in the range $\beta \in [10^{-5}, 10^{-2}]$ using equation (4.14a). The black dashed line in (b) shows the fit of the $Pe = 10^3$ data using equation (4.14b). (c) and (d) show the dependence on β for various Γ at fixed $Pe = 10^2$. The colored dashed lines show the trends predicted by equation (4.14a) (in (c)) and equation (4.14b) (in (d)), using the best-fit coefficients listed in table 1.

Coefficients for γ_{\max}	Coefficients for k_{\max}
$a_0 = -1.89 \pm 0.04$	$b_0 = 9.393 \pm 0.001$
$a_1 = -0.74 \pm 0.02$	$b_1 = -2.8978 \pm 0.0004$
$a_2 = 0.126 \pm 0.003$	

Table 1. Fit coefficients and associated uncertainties obtained from equations (4.14a) and (4.14b) using data for $Pe = 10^3$ and $\beta \in [10^{-5}, 10^{-2}]$ shown in figure 9 (a) and (b). Uncertainties reflect one standard deviation, estimated from the covariance matrix of the fit.

only for a range of parameters that satisfies the assumption of high enough Pe and small enough β .

First, we note that γ_{\max} decreases monotonically with increasing β across all combinations of parameters, eventually becoming negative, as we can see from figure 9 and

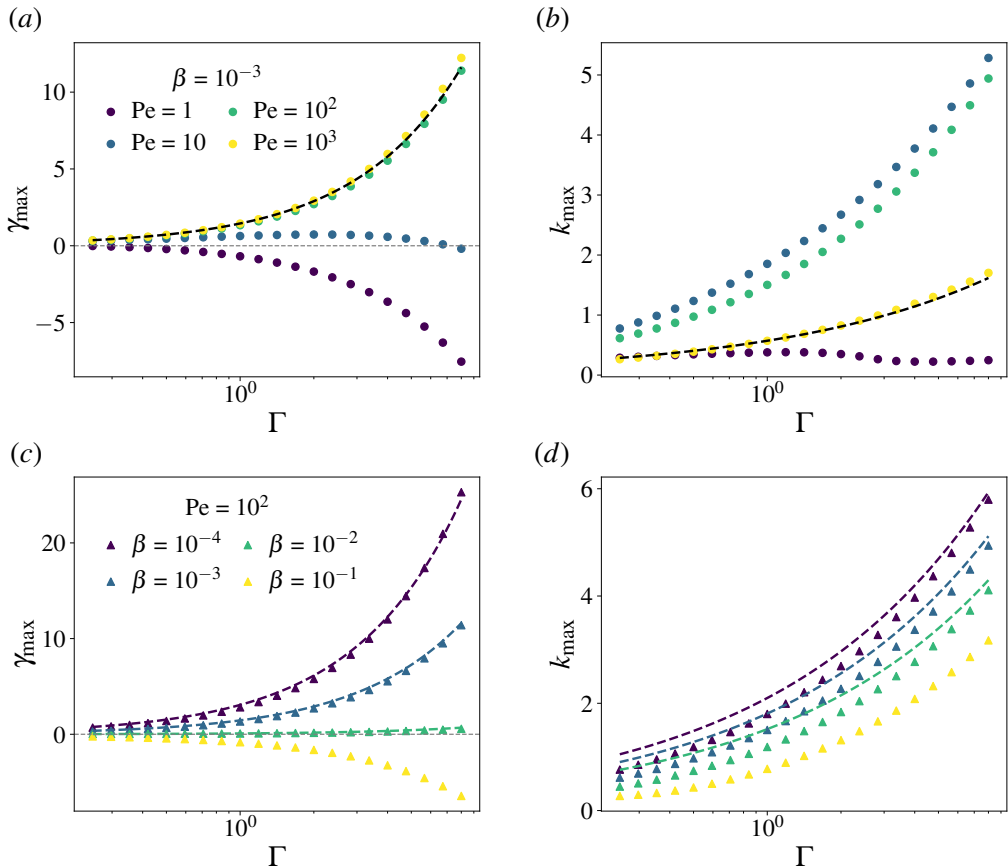


Figure 10. Maximum growth rate γ_{\max} ((a) and (c)) and corresponding wavenumber k_{\max} ((b) and (d)) as functions of the cooling rate $\Gamma \in [0.25, 8]$. Panels (a) and (b) show the dependence on Γ for various Pe at fixed $\beta = 10^{-3}$. The black dashed lines are predictions in the large Pe limit for (a) γ_{\max} and (b) k_{\max} . Panels (c) and (d) show the dependence on Γ for various β at fixed $Pe = 10^2$. The colored dashed lines show the large- Pe predictions for (c) γ_{\max} and (d) k_{\max} . The predictions for γ_{\max} are given by equation (4.14a), and the predictions for k_{\max} are given by equation (4.14b), both using the coefficients listed in table 1.

figure 11(c). This confirms that stronger viscosity contrasts promote the onset and growth of instabilities. The dependence of γ_{\max} on β predicted by equation (4.14a) is corroborated by a quadratic fit of $(\log \beta, \gamma_{\max})$ only for the data for which $Pe = 10^3$ and $\beta \in [10^{-5}, 10^{-2}]$, for which the assumption of high Pe and low β is satisfied, as shown in figure 9(a). The fitted coefficients are reported in table 1. These values are robust when changing Γ , as illustrated by the colored dashed lines in figure 9(c), which agree well with the corresponding numerical data. Moreover, for sufficiently large β , we observe that γ_{\max} remains negative regardless of Pe and Γ . We will discuss this aspect further in § 4.4.

The wavenumber k_{\max} also decreases monotonically with β , but exhibits a distinct linear trend on a semi-logarithmic scale. Specifically, figure 9(b) shows a fit of $(\log \beta, k_{\max})$ for $Pe = 10^3$ and $\beta \in [10^{-5}, 10^{-2}]$ using equation (4.13b). The linear slope is reproduced in figure 9(d) for varying Γ using the same fit parameters, confirming the predictive power of the equation. These results indicate that lower viscosity ratios make the most unstable wavelengths progressively shorter.

Thermal fingers in cold channels: Thermo-viscous instability in dispersive flow

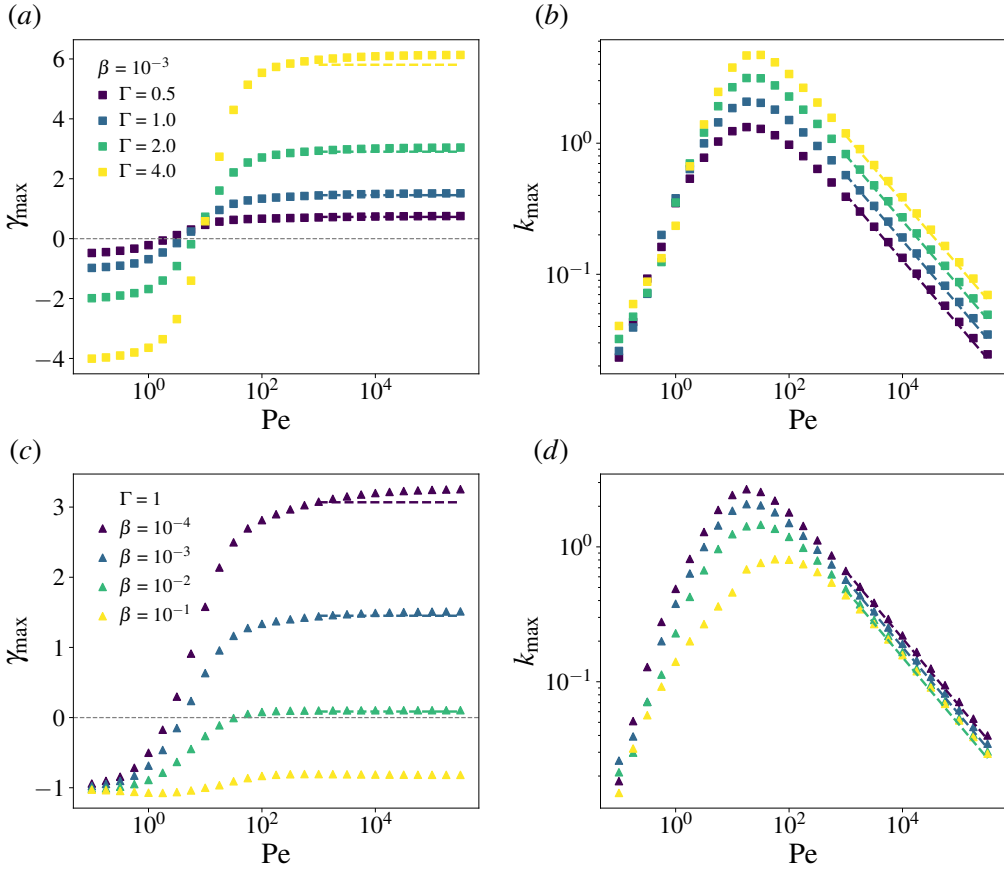


Figure 11. Maximum growth rate γ_{\max} ((a) and (c)) and corresponding wavenumber k_{\max} ((b) and (d)) as functions of the Péclet number $Pe \in [10^{-1}, 10^{5.5}]$. Panels (a) and (b) show the dependence on Pe for various Γ at fixed $\beta = 10^{-3}$. The dashed lines show the large- Pe predictions for (a) γ_{\max} and (b) k_{\max} with colors matching those of the corresponding data for each Γ . Panels (c) and (d) show the dependence on Pe for various β at fixed $\Gamma = 1$. The dashed lines indicate the trends predicted in the limit of large Pe for (c) γ_{\max} and (d) k_{\max} with colors matching those of the corresponding data for each β . The predictions for γ_{\max} are based on equation (4.14a) and the predictions for k_{\max} are based on equation (4.14b), both with coefficients listed in table 1.

Moving further, we observe that, interestingly, Γ does not impact the stability of the injection but only the growth or decay rate of the perturbation, that both monotonically increases with Γ (Figure 10 and figure 11(a)). A notable exception is the set of parameters ($\beta = 10^{-3}, Pe = 10$) that sits at the transition between the stable and unstable regime and for which γ_{\max} has a non-monotonic evolution with Γ and the growth rate changes sign. The cases $Pe = 10^3, \beta = 10^{-3}$ in figure 10(a) and $Pe = 10^2, \beta = \{10^{-4}, 10^{-3}, 10^{-2}\}$ in figure 10(c) are compared with the analytical prediction of equation (4.13a) setting the coefficients to the values of table 1, finding a good agreement.

The monotonic growth of the corresponding values of k_{\max} is visible in figure 10(b) and figure 10(d). Higher cooling rates leads to shorter wavelengths for the fastest mode. In particular the good accuracy of the high- Pe , low- β prediction of equation (4.13b) is highlighted by the black dashed line in figure 10(b) and the colored lines in figure 10(d).

Finally, focusing on the effect of Péclet number on the stability of the system, we observe that γ_{\max} features a low- Pe regime and a high- Pe regime (Figure 11). Except at the transition between these two regimes ($Pe \sim 10$), γ_{\max} evolves weakly with Pe . This suggests that molecular diffusion has a stabilizing effect that is suppressed when advection become dominant.

Where Taylor dispersion does not have an effect on the growth rate, it does impact k_{\max} and promotes perturbation with smaller wavenumber. Overall, k_{\max} displays a non-monotonic trend for all combinations of Γ and β , resembling an asymmetric bell-shaped curve. Increasing Γ results in higher values of k_{\max} throughout the entire range of Pe , without significantly changing the peak position, that is, the value of Pe at which k_{\max} reaches its maximum. In contrast, decreasing β also leads to higher k_{\max} , but in this case shifting the peak toward lower Pe values.

We also report in figure 11 the analytical predictions for γ_{\max} and k_{\max} coming from equations (4.13a) and (4.13b), respectively, adopting (4.14) with the coefficients reported in table 1, for a selected interval of high Pe . The saturation of γ_{\max} with Pe as well as the decay of $k_{\max} \sim Pe^{-1/2}$ are well confirmed for $Pe \gtrsim 10^3$.

4.4. Critical viscosity ratio

An important distinction between thermally driven fingering and the classical Saffman–Taylor instability lies in the existence of a critical viscosity ratio $\beta_c \ll 1$ for the onset of thermal fingering. This threshold has been confirmed through theoretical and numerical analyses (Helfrich 1995; Wylie & Lister 1995; Diniega *et al.* 2013) as well as experimental observations (Holloway & de Bruyn 2005). In contrast, the Saffman–Taylor instability is triggered whenever the viscosity of the displacing fluid is lower than that of the displaced fluid, i.e. when the viscosity ratio is less than one (Saffman & Taylor 1958). Similarly, in the case of miscible viscous fingering, instabilities arise as soon as the mobility ratio, governed by the concentration-dependent viscosity, falls below unity, even in the presence of nonlinear chemical reactions (Tan & Homsy 1986, 1988; De Wit & Homsy 1999).

As seen in § 4.3, the value of β at which the system becomes unstable generally depends on the Péclet number Pe . However, as previously discussed, the growth rate γ_{\max} saturates at a constant value for sufficiently high Pe . We therefore expect the critical viscosity ratio β_c , to converge to a specific value as $Pe \rightarrow \infty$.

In figure 12, we plot β_c as a function of Pe for different values of the cooling rate Γ . Each value of β_c is obtained by performing a quadratic fit over several pairs of $(k_{\max}, \gamma_{\max})$ sampled near the transition between stable and unstable regimes and then extrapolating the value of β corresponding to $\gamma_{\max} = 0$ from the best-fit curve.

We observe that β_c increases with Pe for all values of Γ and tends monotonically toward a limiting value. The asymptotic value we find is $\ln \beta_c = -4.40$, which is close to that reported by Helfrich (1995) ($\ln \beta_c = -4.27$), who studied a system in the limit $Pe \gg 1$ but neglected thermal diffusion and Taylor dispersion.

Physically, this result implies that when advection dominates over thermal diffusion, the system becomes unstable only if the viscosity ratio satisfies $\beta < \beta_c \simeq 0.0123$.

4.5. Comparison between linear stability analysis and nonlinear simulations

To assess the predictive power of the linear theory, we compare its results with those obtained from nonlinear simulations. Figure 13 shows the growth rate of the fastest mode and its wavenumber as functions of the Péclet number Pe , for fixed values $\Gamma = 1$ and $\beta = 10^{-3}$.

The linear stability predictions γ_{\max} and k_{\max} are compared with the corresponding values γ_* and k_* extracted from the full simulations, as described in § 3.2. The two sets of

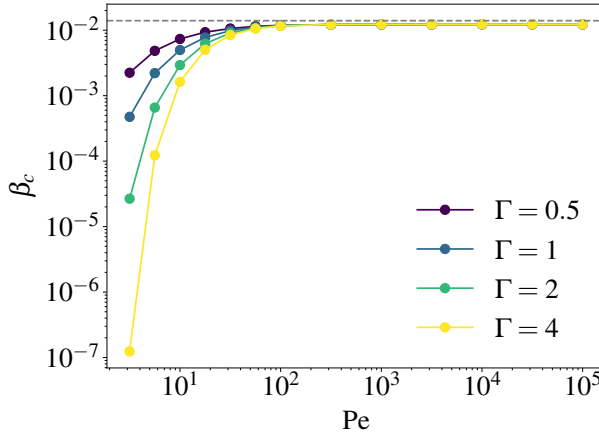


Figure 12. Critical viscosity ratio β_c , above which the system is always stable, as a function of Péclet number Pe for different choices of Γ . The horizontal dotted line shows the value $-\ln \beta_c = 4.27$ reported by Helfrich (1995), close to our value $-\ln \beta_c = 4.4$ estimated in the limit $Pe \rightarrow \infty$.

results are in excellent agreement across the entire range of Pe considered, i.e. $\gamma_{\max} \approx \gamma_*$ and $k_{\max} \approx k_*$. The error bars of the measured wavenumber $k_* = 2\pi n_f / L_y$ shown in figure 13(b) are estimated by taking into account the finite size L_y of the domain in the full simulations. In particular, we assume that the error $\Delta k_* = 2\pi \Delta n_f / L_y = \pm 2\pi / L_y$ reflects that the error in the number of fingers n_f may be up to $|\Delta n_f| = 1$ due to L_y not being a multiple of the theoretical optimal wavelength $2\pi / k_{\max}$. The most unstable wavenumber computed from the linearized model is generally within these error bars. We also note that the measured growth rate, shown in figure 13(a) is systematically slightly below the maximal growth rate based on the linearized model. This behavior can be explained by finite-size effects; as the full model is based on a system size L_y , the actual wavenumber measured, k_* , will be somewhat away from the theoretical optimum k_{\max} (consistent with figure 13(a)) and thus the actual growth rate measured, γ_* , will be somewhat below the theoretical maximum γ_{\max} . This emphasizes that when comparing to experiments or simulations in finite systems, γ_{\max} should be viewed as an upper bound for the growth rate.

The excellent agreement between the full and linearized models confirms that the linear stability analysis accurately captures the dominant features of the instability during its early evolution, including both the characteristic growth rate and the selected wavelength.

5. Discussion and conclusion

In this article, we investigate an instability that arises when hot fluid is injected into a narrow channel conducting heat to a cold surrounding environment. The instability is reminiscent the Saffman–Taylor kind, as it results from the displacement of a more viscous (cold) fluid by a less viscous (hot) one. Like in the Saffman-Taylor instability, larger contrast in viscosity (β in our notation) promotes instability with faster growth rate and smaller unstable wavelengths.

Unlike the classical Saffman–Taylor problem, where two immiscible phases interact (Saffman & Taylor 1958), there is no surface tension at play, and the problem is therefore closer to the dispersive/diffusive instability problem previously studied (Tan & Homsy 1986; Zimmerman & Homsy 1992). Here, the stabilizing mechanism is driven by heat transfer that reduces the temperature of the injected fluid, and thereby the viscosity contrast.

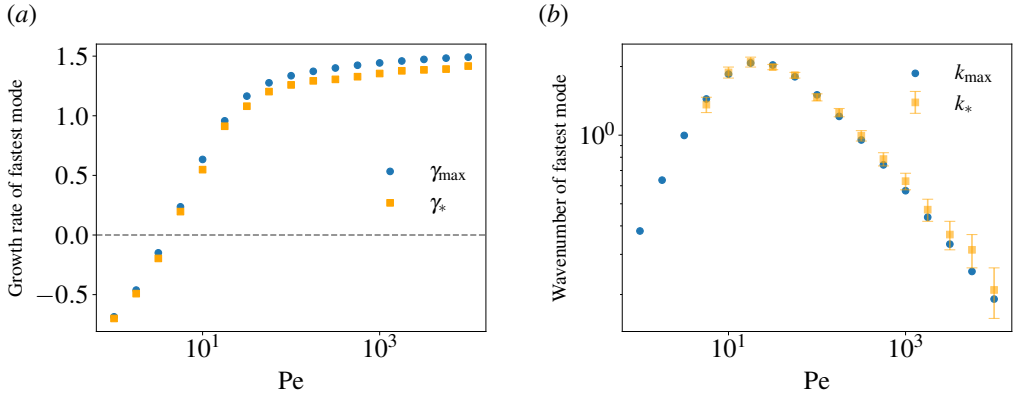


Figure 13. (a) Growth rate of the fastest mode and (b) corresponding wavenumber as functions of the Péclet number Pe in the range $[1, 10^4]$, for $\Gamma = 1$ and $\beta = 10^{-3}$. Results from linear stability analysis are shown as blue circles, while values extracted from nonlinear simulations are shown as orange squares. The error bars on k_* reflect the finite system size in full simulations and are estimated to $\pm 2\pi/L_y$, where $L_y = 60$ is the transverse domain length.

In our Hele-Shaw cell, heat is transferred via four mechanisms: (i) fluid advection, (ii) in-plane thermal diffusion, (iii) hydrodynamic (Taylor) dispersion along the flow direction, and (iv) out-of-plane heat loss through the boundary walls. Due to heat loss, the temperature field is not conserved, in contrast to the classical Saffman-Taylor problems.

Through linear stability analysis, we show that the intricacy of these four mechanisms gives rise to a dispersion relation different from the ones reported for Saffman-Taylor and miscible viscous fingering problems, and relies on the three global parameters: Péclet number, cooling rate, and viscosity ratio.

We demonstrate that the maximum growth rate and most unstable wavenumber of the instability are respectively mediated by a characteristic time Γ^{-1} and a characteristic length scale ξ^{-1} . The former characterizes out-of-plane heat flux through the walls, whereas the latter results from a combination of in-plane molecular diffusion, Taylor dispersion, and heat flux through the walls. Remarkably, these scales are physically related to the solution of two homogeneous problems respectively. The first problem corresponds to that of a homogeneous reservoir under hydrostatic conditions, for which equation (2.14c) can be simplified to $dT/dt = -\Gamma T$, which with the initial condition $T(t = 0) = 1$ leads to the solution $T(t) = e^{-\Gamma t}$; Γ constitutes then the exponential decay rate of the temperature. The second problem is the steady state one-dimensional problem shown in § 2.2, whose solution can be found in equation (2.16), where ξ corresponds to the exponential decay length of the temperature profile.

We find that, in the asymptotic regime of large Pe and small β , the maximum growth rate is governed by the heat transfer coefficient and the viscosity ratio alone, while the corresponding wavelength scales as the inverse of the characteristic length of the base state, $\xi \sim \Gamma^{1/2} Pe^{-1/2}$. We combine equations (4.13) and (4.14) in a dimensional form, writing the maximal growth rate $\gamma_{\max}^{\text{dim}}$ and the most unstable wavelength k_{\max}^{dim} in terms of

the physical quantities characterizing the problem:

$$\gamma_{\max}^{\dim} \stackrel{Uh \gg \kappa, \beta \ll 1}{\simeq} \frac{H}{h\rho c} (a_2 \log^2 \beta + a_1 \log \beta + a_0), \quad (5.1a)$$

$$k_{\max}^{\dim} \stackrel{Uh \gg \kappa, \beta \ll 1}{\simeq} \frac{1}{U\rho c} \sqrt{\frac{H\alpha}{h^3}} (b_1 \log \beta + b_0). \quad (5.1b)$$

We recall that U is the mean flow velocity, h is the half-height of the Hele-Shaw cell, α is the thermal conductivity of the fluid, ρ is its density, c is its specific heat capacity, and the numerical constants a_i, b_i are summarized in table 1. Equations (5.1) can be tested directly against experiments or compared with field data in a geological setting.

We show that the stability of the system is governed by a critical β_c and Péclet number Pe , such that the system is unconditionally stable if $\beta > \beta_c(Pe)$. For large Péclet numbers, we found numerically $\ln \beta_c = -4.4$ (see figure 12), in good agreement with previous work that neglects the effect of thermal diffusivity (Helfrich 1995). This agreement is rather remarkable as our high Péclet number limit corresponds to a strong smearing of the temperature front by Taylor dispersion- an effect that is entirely ignored in Helfrich's model.

Further extensions of the present model could take into account viscous friction heating (Costa & Macedonio 2005), which, in the context of viscous fingering, may contribute in stabilizing the system due to the increase in temperature and consequent reduction in mobility in the displaced fluid, decreasing the viscosity contrast between the invading and displaced fluid (Norouzi *et al.* 2019). Also, taking into account yield stress in the model might be of interest, as, for example, magmatic flow can crystallize and transition to a Bingham flow (Dragoni *et al.* 2002; Castruccio *et al.* 2013). In this case, the instability should be favored, since the cooled fluid would be slowed even more than predicted by the Newtonian flow model.

Acknowledgements. We acknowledge the contribution of Beatrice Baldelli who performed early exploratory simulations of our problem. We are grateful to Hans Jørgen Kjøll, Olivier Galland, and Renaud Toussaint for fruitful discussions.

Funding. This work was supported by the Research Council of Norway through its Center of Excellence funding scheme (PoreLab, project 262644), and through its Researcher Project for Young Talents programme (M4, project 325819, and UNLOC, project 345008).

Declaration of interest. The authors report no conflict of interest.

Data availability statement. The code and scripts used to run simulations, analyze data and produce the figures of this publication will be archived on GitHub (Lanza *et al.* 2025) and will be made accessible and usable at the time of publication.

Author ORCIDs. F. Lanza, <https://orcid.org/0000-0002-5081-9319>; G. Linga, <https://orcid.org/0000-0002-0987-8704>; F. Barras, <https://orcid.org/0000-0003-1109-0200>; E. G. Flekkøy, <https://orcid.org/0000-0002-6141-507X>

Author contributions. **F. Lanza:** Data curation (lead); Formal analysis (equal); Investigation (lead); Software (equal); Validation (lead); Visualization (lead); Writing - original draft (lead). **G. Linga:** Conceptualisation (equal); Formal analysis (equal); Methodology (equal); Software (equal); Validation (supporting); Writing - original draft (supporting); Writing - review & editing (equal); **F. Barras:** Conceptualisation (equal); Formal analysis (equal); Methodology (supporting); Writing - review & editing (equal); **E. G. Flekkøy:** Conceptualisation (equal); Formal analysis (supporting); Funding acquisition (equal); Methodology (equal); Project administration (lead); Supervision (lead); Writing - review & editing (supporting).

Appendix A. Averaging procedure

We recall the governing equations

$$\nabla \cdot \mathbf{u} = 0, \quad (\text{A } 1)$$

$$\nabla \cdot [2\mu(T)\boldsymbol{\varepsilon}] = \nabla p, \quad (\text{A } 2)$$

$$\frac{\partial T}{\partial t} + \mathbf{u} \cdot \nabla T - \kappa \nabla^2 T = 0. \quad (\text{A } 3)$$

We define the pressure, velocity and temperature field averaged along the z -direction

$$p_{\parallel} = \frac{1}{2h} \int_{-h}^h p(x, y, z) dz, \quad \mathbf{u}_{\parallel} = \frac{1}{2h} \int_{-h}^h \mathbf{u}(x, y, z) dz, \quad T_{\parallel} = \frac{1}{2h} \int_{-h}^h T(x, y, z) dz \quad (\text{A } 4)$$

We recall that we assume laminar flow through all the domain, so $p = p_{\parallel}$ and the velocity field \mathbf{u} can be written as

$$\mathbf{u} = \frac{3}{2} \mathbf{u}_{\parallel} \left(1 - \left(\frac{z}{h} \right)^2 \right) \quad (\text{A } 5)$$

where h is half the cell thickness.

For the incompressibility condition (A 1), we have $\nabla \cdot \mathbf{u} = \nabla_{\parallel} \cdot \mathbf{u}_{\parallel} = 0$, where we defined $\nabla_{\parallel} = \hat{\mathbf{e}}_x \partial_x + \hat{\mathbf{e}}_y \partial_y$.

For the Darcy law (A 2), using (A 1) we can rewrite the left-hand side:

$$\nabla \mu(T) \cdot (\nabla \mathbf{u} + \nabla \mathbf{u}^{\top}) + \mu(T) \nabla^2 \mathbf{u} = \nabla p. \quad (\text{A } 6)$$

From the laminar flow profile (A 5), we then have

$$\frac{3}{2} \left(1 - \left(\frac{z}{h} \right)^2 \right) \left(\nabla \mu(T) \cdot (\nabla \mathbf{u}_{\parallel} + \nabla \mathbf{u}_{\parallel}^{\top}) + \mu(T) \nabla^2 \mathbf{u}_{\parallel} \right) - \frac{3}{h^2} \mu(T) \mathbf{u}_{\parallel} = \nabla p. \quad (\text{A } 7)$$

We now average both sides of the equation along z . Assuming laminar flow in the cell implies $p = p(x, y)$, so the average of the pressure gradient gives $\nabla_{\parallel} p_{\parallel}$. On the other hand, we are assuming that the temperature changes in the direction perpendicular to the plates are negligible with respect to the ones in the perpendicular direction, so that the z -averaged viscosity is

$$\frac{1}{2h} \int_{-h}^h \mu(T(z)) dz \simeq \frac{1}{2h} \int_{-h}^h \mu(T_{\parallel}) dz = \mu(T_{\parallel}). \quad (\text{A } 8)$$

These considerations lead to the following flow equation

$$\left(\nabla \mu(T_{\parallel}) \cdot (\nabla \mathbf{u}_{\parallel} + \nabla \mathbf{u}_{\parallel}^{\top}) + \mu(T) \nabla^2 \mathbf{u}_{\parallel} \right) - \frac{3}{h^2} \mu(T) \mathbf{u}_{\parallel} = \nabla p. \quad (\text{A } 9)$$

If we now adopt the lubrication approximation, for which $|\nabla \mathbf{u}_{\parallel}| \ll |\mathbf{u}_{\parallel}|/h$, and we assume viscosity gradients to be small such that $|\nabla \mu| \ll \mu/h$, we obtain a linear relationship between the 2D pressure gradient and the corresponding velocity field:

$$-\frac{3}{h^2} \mu(T_{\parallel}) \mathbf{u}_{\parallel} = \nabla_{\parallel} p_{\parallel}. \quad (\text{A } 10)$$

We now discuss the averaging of the advection-diffusion equation (A 3). We will follow a derivation based on large-time asymptotics (Liñán *et al.* 2020) applied to our planar geometry. For simplicity, we adopt a reference system for which the local velocity is directed toward x , namely $\mathbf{u}_{\parallel} = (u, 0)$ where u is the mean velocity modulus. Suppose the fluid has a temperature distribution T introduced into the pipe at $t = 0$ with an arbitrary initial profile. If this initial temperature distribution is compact (i.e., the temperature has a localized variation and is not uniform throughout the pipe), the temperature field will be convected along the pipe at the mean velocity u . We adopt a frame moving with the mean velocity and scaled with following non-dimensional scales

$$t' = \frac{t}{h^2/\kappa}, \quad x' = \frac{x - ut}{h}, \quad z' = \frac{z}{h}, \quad Pe = \frac{uh}{\kappa} \quad (\text{A } 11)$$

where κ is the thermal diffusivity of the fluid, h^2/κ is the characteristic time for the temperature to diffuse across the channel and Pe is the thermal Péclet number. In this way, equation (A 3) becomes

$$\frac{\partial T}{\partial t'} + Pe(1 - 2z'^2) \frac{\partial T}{\partial x'} - \frac{\partial^2 T}{\partial x'^2} - \frac{\partial^2 T}{\partial z'^2} = 0 \quad (\text{A } 12)$$

In this moving frame, at times $t' \sim 1$ (in dimensional variables, $t \sim h^2/\kappa$), the temperature will diffuse vertically within the cell. For $t' \gg 1$ (in dimensional variables, $t \gg h^2/\kappa$), thermal diffusion will cause the temperature

Thermal fingers in cold channels: Thermo-viscous instability in dispersive flow

to become uniform along the vertical direction, although temperature gradients along the x -direction may still persist, for which the related diffusion process is described by Taylor dispersion. If $t' \sim 1/\epsilon \gg 1$, where $\epsilon \ll 1$ (namely, times much greater than the out-of-plane diffusion time h^2/κ), the temperature field will have spread along x over a distance $x \sim \sqrt{t} \sim \sqrt{1/\epsilon} \gg 1$. To quantify large-time behavior, the following rescaling can be introduced:

$$\tau = \epsilon t', \quad \zeta = \sqrt{\epsilon} x', \quad (\text{A } 13)$$

Equation (A 12) is then rewritten as

$$\epsilon \frac{\partial T}{\partial \tau} + \sqrt{\epsilon} Pe(1 - 2z'^2) \frac{\partial T}{\partial \zeta} - \epsilon \frac{\partial^2 T}{\partial \zeta^2} - \frac{\partial^2 T}{\partial z'^2} = 0 \quad (\text{A } 14)$$

Since $\epsilon \ll 1$, the solution can be expanded in an asymptotic series, $T = T_0 + \sqrt{\epsilon} T_1 + \epsilon T_2 + \dots$

To leading order, equation (A 14) becomes

$$\frac{\partial^2 T_0}{\partial z'^2} = 0 \quad (\text{A } 15)$$

which, together with the symmetry condition $\frac{\partial T}{\partial z'}|_{z'=0} = 0$, gives $T_0 = T_0(\xi, \tau)$, namely T_0 is independent of z' . This is a direct consequence of the thermal diffusion that, at large times, makes the concentration uniform across the cell. Note that $T_0 = T_{\parallel}$ as defined in (A 4). To order $\sqrt{\epsilon}$ we have

$$Pe(1 - 2z'^2) \frac{\partial T_{\parallel}}{\partial \zeta} - \frac{\partial^2 T_1}{\partial z'^2} = 0 \quad (\text{A } 16)$$

which, together with the condition $\frac{\partial T}{\partial z'}|_{z'=0} = 0$ gives

$$T_1(\xi, z', \tau) = Pe \frac{z'^2}{2} \left(1 - \frac{z'^2}{3} \right) \frac{\partial T_{\parallel}}{\partial \zeta} + T_{1,z'=0} \quad (\text{A } 17)$$

where $T_{1,z'=0}$ is the unknown value of T_1 at $z' = 0$. The following equation is obtained at order ϵ :

$$\frac{\partial T_{\parallel}}{\partial \tau} - \frac{\partial^2 T_{\parallel}}{\partial \zeta^2} + Pe(1 - 2z'^2) \frac{\partial T_1}{\partial \zeta} - \frac{\partial^2 T_2}{\partial z'^2} = 0. \quad (\text{A } 18)$$

This can be solved by averaging it over the cell thickness, i.e. integrating it between $z' = 0$ and 1. Applying (A 17) and the boundary conditions $\frac{\partial T}{\partial z'}|_{z'=0} = 0$ and $\frac{\partial T}{\partial z'}|_{z'=1} = (Hh/\alpha)(T_c - T_{\parallel})$ (the latter coming from (2.7)), we obtain

$$\frac{\partial T_{\parallel}}{\partial \tau} - \frac{\partial^2 T_{\parallel}}{\partial \zeta^2} \left(1 + \frac{2Pe^2}{105} \right) + \frac{Hh}{\alpha\epsilon} (T_{\parallel} - T_c) = 0 \quad (\text{A } 19)$$

Returning to the original coordinates, the equation becomes

$$\frac{\partial T_{\parallel}}{\partial t} + u \frac{\partial T_{\parallel}}{\partial x} - \kappa \frac{\partial^2 T_{\parallel}}{\partial x^2} \left(1 + \frac{2U^2 h^2}{105\kappa^2} \right) + \frac{H}{h\rho c} (T_{\parallel} - T_c) = 0 \quad (\text{A } 20)$$

where T_{\parallel} is as defined in (A 4). Generalizing for any direction parallel to the cell plates:

$$\frac{\partial T_{\parallel}}{\partial t} + \mathbf{u}_{\parallel} \cdot \nabla_{\parallel} T_{\parallel} - \nabla_{\parallel} \cdot (\mathbf{D} \nabla_{\parallel} T_{\parallel}) + \frac{H}{h\rho c} (T_{\parallel} - T_c) = 0 \quad (\text{A } 21)$$

where the anisotropic dispersion is represented by a 2×2 tensor:

$$\mathbf{D} = \kappa \left(\mathbf{I} + \frac{2}{105} \left(\frac{h}{\kappa} \right)^2 \mathbf{u}_{\parallel} \otimes \mathbf{u}_{\parallel} \right). \quad (\text{A } 22)$$

Appendix B. Numerical method

B.1. Fully coupled model

We solve the fully coupled model 2.14 using a finite element method. We use a semi-implicit first-order time-splitting scheme formulated in the following.

We define Ω as the domain $\mathbf{x} \in [0, L_x] \times [0, L_y]$, as sketched in figure 1(b), discretized into a quadrilateral grid. We further define the scalar function space S as the space of Q_1 functions on this grid.

The time-stepping scheme is given by:

- (i) Initialize $T^0 \in S$ according to the base state (2.16). Set the iteration index $n = 1$.
- (ii) Find $p^n \in S$ such that for all $b \in S$,

$$\int_{\Omega} \beta^{-T^{n-1}} \nabla p^n \cdot \nabla b \, d^2x = \int_0^{L_y} u_x(0, y, t) b(0, y) \, dy, \quad (\text{B } 1)$$

where $u_x(0, y, t)$ is given by equations (3.1) or (3.4), subject to the Dirichlet boundary condition $p^n(L_x, y, t) = 0$.

- (iii) Find $T^n \in S$ such that for all $b \in S$,

$$\begin{aligned} \frac{1}{\Delta t} \int_{\Omega} T^n b \, d^2x + \int_{\Omega} \mathbf{u}^n \cdot \nabla T^n b \, d^2x + \frac{1}{Pe} \int_{\Omega} \nabla T^n \cdot \nabla b \, d^2x \\ + \frac{2Pe}{105} \int_{\Omega} (\mathbf{u}^n \cdot \nabla T^n)(\mathbf{u}^n \cdot \nabla b) \, d^2x + \Gamma \int_{\Omega} T^n b \, d^2x = \frac{1}{\Delta t} \int_{\Omega} T^{n-1} b \, d^2x, \end{aligned} \quad (\text{B } 2)$$

where Δt is the time step, $T^n(0, y, t) = 1$, and

$$\mathbf{u}^n = -\beta^{-T^{n-1}} \nabla p^n \quad (\text{B } 3)$$

is the estimated velocity based on previously computed values.

- (iv) Stop the simulation if $n\Delta t \geq t_{\text{tot}}$, where t_{tot} is the predefined total simulation time. Otherwise, increase $n \leftarrow n + 1$ and repeat from step (ii).

We implement the scheme above in FEniCSx 0.9.0 (Baratta *et al.* 2023) using periodic boundary conditions at $y = 0$ and $y = L_y$. We solve both equations numerically using iterative solvers: equation (B 1) using the conjugate gradient method with the Hypre BoomerAMG preconditioner (Yang *et al.* 2002), equation (B 2) using the stabilized bi-conjugate gradient method with a Jacobi preconditioner.

The implementation can be found in the Git repository (Lanza *et al.* 2025) in the file `cooling.py`.

B.2. Linearized model

To solve the linearized model (4.6) we use a first-order implicit time-stepping scheme with mixed finite elements. The scheme can be written as the following:

- (i) Initialize $T^0(x)$ according to (2.16). Set $n = 1$.
- (ii) Find $(T^n, u^n) \in W$ such that for all $(Q, v) \in W$:

$$\begin{aligned} \frac{1}{\Delta t} \int_0^{L_x} (T^n - T^{n-1}) Q \, dx + \int_0^{L_x} \frac{dT^n}{dx} Q \, dx + \kappa_{\text{eff}} \int_0^{L_x} \frac{dT^n}{dx} \frac{dQ}{dx} \, dx \\ + (\kappa k^2 + \Gamma) \int_0^{L_x} T^n Q \, dx + \xi \int_0^{L_x} T_0(x) \left[-(1 + 2\kappa_{\parallel} \xi) u^n + \kappa_{\parallel} \frac{du^n}{dx} \right] Q \, dx = 0 \end{aligned} \quad (\text{B } 4a)$$

and

$$- \int_0^{L_x} \frac{du^n}{dx} \frac{dv}{dx} \, dx + \psi \xi \int_0^{L_x} T_0(x) \frac{du^n}{dx} v \, dx - k^2 \int_0^{L_x} u^n v \, dx + k^2 \psi \int_0^{L_x} T^n v \, dx = 0 \quad (\text{B } 4b)$$

under the Dirichlet boundary conditions $T^n(0) = 0$ and $u^n(0) = \epsilon \Theta(t_{\text{pert}} - t)$ where Θ is the Heaviside step function.

- (iii) If $n\Delta t \geq t_{\text{tot}}$, where t_{tot} is the total simulation time, stop the simulation. Otherwise, increase $n \rightarrow n + 1$ and go to step (ii).

The equation system (B 4) is solved using FEniCS 2019.2.0 (Logg *et al.* 2012) by means of a direct solver (LU factorization). The implementation can be found in the Git repository (Lanza *et al.* 2025) in the file `linear_model.py`.

B.3. Mesh length and resolution

To perform simulations of the linearized model, we need to specify the length of the one-dimensional domain L_x , the number of tiles along it N_x , the time step δt and the total simulation time t_{tot} .

We can derive a rough estimate of the solution profile length from the inverse of the characteristic length of the base state ξ , defined in equation (2.17). Given a value for the cooling rate Γ and the Péclet number Pe , we can compute ξ from (2.17). Hence, we choose to set the domain length to $L_x = 10/\xi$. Since the maximum of T_x located at the beginning of the domain, as visible in figure 7, the ratio between its peak value and its value at the end of the domain, $x = L_x$, can be estimated as $\max_x \hat{T}_k(x)/T_k(x = L_x) \simeq e^{10}$. This indicates that the tail

Thermal fingers in cold channels: Thermo-viscous instability in dispersive flow

of the temperature perturbation decays by approximately four orders of magnitude across the chosen domain length, ensuring that boundary effects at $x = L_x$ remain negligible.

The number of tiles N_x was specified such as the mesh resolution was constant for all simulations and equal to $N_x/L_x = 10$. Moreover, the time step was set to $\delta t = 0.005$. Both choices are motivated by observing that, respectively, higher values for N_x/L_x , or lower values of δt , would alter the measured value of γ by a relative change $\varepsilon_{\text{rel}} \lesssim 10^{-4}$, which we consider acceptable for our purposes.

We see that, by setting the perturbation time to $t_{\text{pert}} = 0.1$, the linear growth regime is reached at $t \sim 5$ at the latest (see figure 6). Hence, for all the simulations performed, the total time was set to $t_{\text{tot}} = 20$; this choice produce a time interval sufficiently large for calculating γ as the slope of the best fit's curve in an interval corresponding to the linear growth regime.

With respect to the linearized model, for the full non-linear simulations we also need to specify the length of the domain along the y -axis L_y , and the number of rectangular tiles N_y along it. Being the imposed perturbation variation along the y -axis, a mesh resolution along y higher than along x is in general needed. For the simulations with random perturbation at the inlet we performed in this work, we set $L_y = 60$, $N_x/L_x = 2$, $N_y/L_y = 50$, $\delta t = 0.005$. L_x and t_{tot} varied depending on Pe . This choice allowed to obtain a good agreement between the measured values of γ_* (k_*) and the corresponding values of γ_{max} (k_{max}) from the linearized model, as we can see from figure 13. For a proper study of the non-linear terms of the solution, a more refined choice is needed. However, this goes beyond the scope of the our present work.

The linearized model was run on a single node with $4 \times$ Intel® Xeon® Gold 6254 CPUs (3.10 GHz, 72 physical cores / 144 threads total) and typically completed in 2–3 minutes. However, to determine (k_{max} , γ_{max}) for a given set of global parameters, we perform multiple simulations at different k -values followed by a quadratic fit, as explained in § 4.3. As a result, exploring each global parameter combination requires a few hours of computation time. In contrast, full non-linear simulations were executed using 64 MPI processes and took several hours each on average. Depending on the scheduler configuration, these parallel simulations may have utilized one or more nodes.

Appendix C. Large Pe limit of the linearized model

We consider the linearized equations (4.9), inserting $T_0 = e^{-\xi x}$:

$$\left(\frac{d^2}{dx^2} + \psi \xi e^{-\xi x} \frac{d}{dx} - k^2 \right) \hat{u}_k = -k^2 \psi \hat{T}_k, \quad (\text{C } 1a)$$

$$\left(\gamma + \frac{d}{dx} - \kappa_{\text{eff}} \frac{d^2}{dx^2} + \kappa k^2 + \Gamma \right) \hat{T}_k = \xi e^{-\xi x} \left(1 + \kappa_{\parallel} \left(2\xi - \frac{d}{dx} \right) \right) \hat{u}_k. \quad (\text{C } 1b)$$

We use the length scale ξ^{-1} to rescale x and k :

$$x = \xi^{-1} \tilde{x}, \quad k = \xi \tilde{k}. \quad (\text{C } 2)$$

Equation (C 1) then becomes:

$$\left(\frac{d^2}{d\tilde{x}^2} + \psi e^{-\tilde{x}} \frac{d}{d\tilde{x}} - \tilde{k}^2 \right) \hat{u}_k = -\tilde{k}^2 \hat{\tau}_k, \quad (\text{C } 3a)$$

$$\left(\gamma + \xi \frac{d}{d\tilde{x}} - \kappa_{\text{eff}} \xi^2 \frac{d^2}{d\tilde{x}^2} + \kappa \xi^2 \tilde{k}^2 + \Gamma \right) \hat{\tau}_k = \xi \psi e^{-\tilde{x}} \left(1 + \kappa_{\parallel} \xi \left(2 - \frac{d}{d\tilde{x}} \right) \right) \hat{u}_k, \quad (\text{C } 3b)$$

where we defined $\hat{\tau}_k = \psi \hat{T}_k$.

We now assume that $\kappa_{\text{eff}} \gg \Gamma^{-1}$, which implies, recalling from (2.17)

$$\xi = \frac{-1 + \sqrt{1 + 4\Gamma \kappa_{\text{eff}}}}{2\kappa_{\text{eff}}} \simeq \sqrt{\frac{\Gamma}{\kappa_{\text{eff}}}}. \quad (\text{C } 4)$$

We further consider the high Pe limit, which means $\kappa_{\parallel} \gg \kappa$. Combining both assumptions with (C 3) and (C 4), equation (C 3a) remains unchanged while (C 3b) simplifies to

$$\left(\frac{\gamma}{\Gamma} + 1 - \frac{d^2}{d\tilde{x}^2} \right) \hat{\tau}_k = \psi e^{-\tilde{x}} \left(2 - \frac{d}{d\tilde{x}} \right) \hat{u}_k. \quad (\text{C } 5)$$

We see from (C 3a) and (C 5) that the only dimensionless parameters are $\tilde{\gamma} \equiv \gamma/\Gamma$, \tilde{k} and ψ . Hence, the growth rate γ must in the high Pe limit be given by

$$\gamma(k; \Gamma, \kappa_{\parallel}, \psi) = \Gamma \tilde{\gamma}(\tilde{k}; \psi). \quad (\text{C } 6)$$

Since the rescaled dispersion relationship $\tilde{\gamma}(\tilde{k})$ depends only on the parameter ψ , its global maximum and the corresponding wavelength, which we call $\tilde{\gamma}_{\max}$ and \tilde{k}_{\max} respectively, are solely functions of ψ as well. Hence,

$$k_{\max}(\kappa_{\parallel}, \Gamma, \psi) = \sqrt{\frac{\Gamma}{\kappa_{\parallel}}} \tilde{k}_{\max}(\psi), \quad (\text{C7a})$$

$$\gamma_{\max}(\kappa_{\parallel}, \Gamma, \psi) = \gamma(k_{\max}; \kappa_{\parallel}, \Gamma, \psi) = \Gamma \tilde{\gamma}(\tilde{k}_{\max}(\psi); \psi) = \Gamma \tilde{\gamma}_{\max}(\psi), \quad (\text{C7b})$$

In summary, as $Pe \rightarrow \infty$, the asymptotic scalings for the fastest mode and its growth rate are $k_{\max} \sim Pe^{-1/2} \Gamma^{1/2}$ and $\gamma_{\max} \sim \Gamma$, respectively. We further note that as ψ_c is the value of ψ where $\gamma_{\max}(\psi_c) = 0$, it follows that for high Péclet numbers $\beta_c = e^{-\psi_c}$ is a universal numerical value independent of any system parameters.

C.1. Large viscosity ratio

Taking the analysis a step further, we may assume that ψ is *large*. We introduce the scaled quantities $\tilde{k} = \psi^{-1} \tilde{k}$ and $\tilde{x} = \psi \tilde{x}$. Equations (C3a) and (C5) become

$$\left(\frac{d^2}{d\tilde{x}^2} + e^{-\tilde{x}/\psi} \frac{d}{d\tilde{x}} - \tilde{k}^2 \right) \hat{u}_k = -\tilde{k}^2 \hat{\tau}_k, \quad (\text{C8a})$$

$$\left(\frac{\gamma}{\psi^2} + 1 - \frac{d^2}{d\tilde{x}^2} \right) \hat{\tau}_k = e^{-\tilde{x}/\psi} \left(\frac{2}{\psi} - \frac{d}{d\tilde{x}} \right) \hat{u}_k. \quad (\text{C8b})$$

\hat{u}_k will typically decay with x as $\hat{u}_k \sim e^{-\tilde{\eta}\tilde{x}}$ where $\tilde{\eta} = \min\{\tilde{k}, \tilde{\gamma}\}$. Hence, for large ψ , $e^{-\tilde{x}/\psi} \simeq 1$ wherever \hat{u}_k is significant. To the lowest order in the small parameter $1/\psi$, equations (C8) become

$$\left(\frac{d^2}{d\tilde{x}^2} + \frac{d}{d\tilde{x}} - \tilde{k}^2 \right) \hat{u}_k = -\tilde{k}^2 \hat{\tau}_k, \quad (\text{C9a})$$

$$\left(\frac{\gamma}{\psi^2} + 1 - \frac{d^2}{d\tilde{x}^2} \right) \hat{\tau}_k = -\frac{d}{d\tilde{x}} \hat{u}_k. \quad (\text{C9b})$$

Here, all the system parameters are grouped together in the first term of (C9b), which should be solely given by \tilde{k} . This scaling thus explains why $k_{\max} \sim \psi$ and $\sqrt{\gamma_{\max}/\Gamma + 1} \sim \psi$ for large ψ , up to numerical prefactor.

It should be noted that expanding (C8) to the first order in $1/\psi$ would give a more accurate estimate of $k_{\max} \sim \psi(1 + \text{const.}/\psi) \sim \text{const.} + \psi$ (and similar for γ_{\max}). This linear functional form is in excellent agreement with our data for $\psi > \psi_c$.

Appendix D. Relation to the dispersion-free model

As mentioned in § 2.1, a model where in-plane temperature transport is purely advective and thermal dispersion is entirely neglected cannot be obtained as a $Pe \rightarrow \infty$ limit of (C1b). Instead, we can take the artificial dispersion-free limit $\kappa, \kappa_{\parallel} \rightarrow 0$, which through (2.17) becomes

$$\xi = \frac{-1 + \sqrt{1 + 4\Gamma\kappa_{\text{eff}}}}{2\kappa_{\text{eff}}} \simeq \Gamma. \quad (\text{D1})$$

With the scaling (C2), we obtain (C3a) and (C3b). In this case, the latter simplifies to

$$\left(\frac{\gamma}{\Gamma} + 1 + \frac{d}{d\tilde{x}} \right) \hat{\tau}_k = \psi e^{-\tilde{x}} \hat{u}_k. \quad (\text{D2})$$

With the same reasoning as in Appendix C, we can derive a scaling for the fastest mode wavenumber and its growth rate

$$k_{\max}(\Gamma, \psi) = \Gamma \tilde{k}_{\max}^{\text{H}}(\psi), \quad (\text{D3})$$

$$\gamma_{\max}(\Gamma, \psi) = \Gamma \tilde{\gamma}_{\max}^{\text{H}}(\psi). \quad (\text{D4})$$

with $\tilde{k}_{\max}^{\text{H}}(\psi)$ and $\tilde{\gamma}_{\max}^{\text{H}}(\psi)$ are functions of $\psi = -\log \beta$.

REFERENCES

ANDERSON, S.W., MCCOLLEY, S.M., FINK, J.H. & HUDSON, R.K. 2005 The development of fluid instabilities

Thermal fingers in cold channels: Thermo-viscous instability in dispersive flow

- and preferred pathways in lava flow interiors: Insights from analog experiments and fractal analysis. In *Kinematics and dynamics of lava flows*. Geological Society of America.
- ARIS, R. & TAYLOR, GEOFFREY INGRAM 1956 On the dispersion of a solute in a fluid flowing through a tube. *Proceedings of the Royal Society of London. Series A. Mathematical and Physical Sciences* **235** (1200), 67–77, arXiv: <https://royalsocietypublishing.org/doi/pdf/10.1098/rspa.1956.0065>.
- AUSTIN-ADIGIO, MAUREEN & GATES, IAN D. 2020 Thermal viscous fingering in thermal recovery processes. *Energies* **13** (18).
- BARATTA, IGOR A., DEAN, JOSEPH P., DOKKEN, JØRGEN S., HABERA, MICHAL, HALE, JACK S., RICHARDSON, CHRIS N., ROGNES, MARIE E., SCROGGS, MATTHEW W., SIME, NATHAN & WELLS, GARTH N. 2023 Dolfinx: The next generation fenics problem solving environment.
- BLATT, HARVEY, TRACY, ROBERT J. & OWENS, BRENT E. 2006 *Petrology, Igneous, Sedimentary, and Metamorphic*, 3rd edn. New York: W.H. Freeman & Company.
- BOWDEN, F P & TABOR, D 2001 *The Friction and Lubrication of Solids*. Oxford University Press Oxford.
- CASTRUCCIO, ANGELO, RUST, A. C. & SPARKS, R. S. J. 2013 Evolution of crust- and core-dominated lava flows using scaling analysis. *Bulletin of Volcanology* **75** (681).
- COSTA, A. & MACEDONIO, G. 2005 Viscous heating effects in fluids with temperature-dependent viscosity: triggering of secondary flows. *Journal of Fluid Mechanics* **540**, 21–38.
- DE WIT, A. 2020 Chemo-hydrodynamic patterns and instabilities. *Annual Review of Fluid Mechanics* **52** (Volume 52, 2020), 531–555.
- DE WIT, A. & HOMS, G. M. 1999 Viscous fingering in reaction-diffusion systems. *The Journal of Chemical Physics* **110** (17), 8663–8675, arXiv: https://pubs.aip.org/aip/jcp/article-pdf/110/17/8663/19280284/8663_1_online.pdf.
- DINIEGA, S., SMREKAR, S. E., ANDERSON, S. & STOFAN, E. R. 2013 The influence of temperature-dependent viscosity on lava flow dynamics. *Journal of Geophysical Research: Earth Surface* **118** (3), 1516–1532, arXiv: <https://agupubs.onlinelibrary.wiley.com/doi/pdf/10.1002/jgrf.20111>.
- DRAGONI, MICHELE, D'ONZA, FRANCESCA & TALLARICO, ANDREA 2002 Temperature distribution inside and around a lava tube. *Journal of Volcanology and Geothermal Research* **115** (1), 43–51.
- FEDER, J., FLEKKØY, E. G. & HANSEN, A. 2022 *Physics of Flow In Porous Media*, 1st edn. Cambridge: Cambridge University Press.
- GALLAND, OLIVIER, SPACAPAN, JUAN B., RABELL, OLE, MAIR, KAREN, SOTO, FREDERICO GONZÁLEZ, EIKEN, TROND, SCHIUMA, MARIO & LEANZA, HÉCTOR A. 2019 Structure, emplacement mechanism and magma-flow significance of igneous fingers – Implications for sill emplacement in sedimentary basins. *Journal of Structural Geology* **124**, 120–135.
- GHEMAT, KARIM & AZAIEZ, JALEL 2008 Viscous fingering instability in porous media: Effect of anisotropic velocity-dependent dispersion tensor. *Transport in Porous Media* **73** (3), 297–318.
- GRIFFITHS, R. W. 1986 Thermals in extremely viscous fluids, including the effects of temperature-dependent viscosity. *Journal of Fluid Mechanics* **166**, 115–138.
- HELFRICH, KARL R. 1995 Thermo-viscous fingering of flow in a thin gap: a model of magma flow in dikes and fissures. *Journal of Fluid Mechanics* **305**, 219–238.
- HOLLOWAY, KRISTI E & DE BRUYN, JOHN R 2005 Viscous fingering with a single fluid. *Canadian Journal of Physics* **83** (5), 551–564, arXiv: <https://doi.org/10.1139/p05-024>.
- HOLLOWAY, KRISTI E & BRUYN, JOHN R 2006 Numerical simulations of a viscous-fingering instability in a fluid with a temperature-dependent viscosity. *Canadian Journal of Physics* **84** (4), 273–287, arXiv: <https://doi.org/10.1139/p06-052>.
- HOMS, GEORGE M 1987 Viscous fingering in porous media. *Annual review of fluid mechanics* **19** (1), 271–311.
- JHA, BIRENDRA, CUETO-FELGUEROSO, LUIS & JUANES, RUBEN 2011 Fluid mixing from viscous fingering. *Phys. Rev. Lett.* **106**, 194502.
- JONES, T. J., LLEWELLIN, E. W., HOUGHTON, B. F., BROWN, R. J. & VYE-BROWN, C. 2017 Proximal lava drainage controls on basaltic fissure eruption dynamics. *Bulletin of Volcanology* **79** (11), 81.
- KEABLE, DANIEL, JONES, ALISTAIR, KREVER, SAMUEL, MUGGERIDGE, ANN & JACKSON, SAMUEL J. 2022 The effect of viscosity ratio and pecllet number on miscible viscous fingering in a hele-shaw cell: A combined numerical and experimental study. *Transport in Porous Media* **143** (1), 23–45.
- LANZA, FEDERICO, LINGA, GAUTE, BARRAS, FABIAN & FLEKKØY, EIRIK GRUDE 2025 Git repository. <https://github.com/FedericoLanza/cooling-instability/>, 2025-07-02.
- LIÑÁN, AMABLE, RAJAMANICKAM, PRABAKARAN, WEISS, ADAM D. & AND, ANTONIO L. SÁNCHEZ 2020 Taylor-diffusion-controlled combustion in ducts. *Combustion Theory and Modelling* **24** (6), 1054–1069, arXiv: <https://doi.org/10.1080/13647830.2020.1813335>.
- LOGG, ANDERS, MARDAL, KENT-ANDRE & WELLS, GARTH 2012 *Automated solution of differential equations by the finite element method: The FEniCS book*, , vol. 84. Springer Science & Business Media.

- MCDOWELL, ALASTAIR, ZARROUK, SADIQ J. & CLARKE, RICHARD 2016 Modelling viscous fingering during reinjection in geothermal reservoirs. *Geothermics* **64**, 220–234.
- MORRIS, S. J. S. 1996 Stability of thermoviscous hele-shaw flow. *Journal of Fluid Mechanics* **308**, 111–128.
- NAGATSU, YUICHIRO, FUJITA, NORIHIITO, KATO, YOSHIHIITO & TADA, YUTAKA 2009 An experimental study of non-isothermal miscible displacements in a hele-shaw cell. *Experimental Thermal and Fluid Science* **33** (4), 695–705.
- NOROUZI, M., DORRANI, S., SHOKRI, H. & ANWAR BÉG, O. 2019 Effects of viscous dissipation on miscible thermo-viscous fingering instability in porous media. *International Journal of Heat and Mass Transfer* **129**, 212–223.
- PANSINO, S., EMADZADEH, A. & TAISNE, B. 2019 Dike channelization and solidification: Time scale controls on the geometry and placement of magma migration pathways. *Journal of Geophysical Research: Solid Earth* **124** (9), 9580–9599, arXiv: <https://agupubs.onlinelibrary.wiley.com/doi/pdf/10.1029/2019JB018191>.
- POLLARD, DAVID D., MULLER, OTTO H. & DOCKSTADER, DAVID R. 1975 The Form and Growth of Fingered Sheet Intrusions. *GSA Bulletin* **86** (3), 351–363.
- PRAMANIK, SATYAJIT & MISHRA, MANORANJAN 2015 Effect of péclet number on miscible rectilinear displacement in a hele-shaw cell. *Phys. Rev. E* **91**, 033006.
- SAFFMAN, PHILIP GEOFFREY & TAYLOR, GEOFFREY INGRAM 1958 The penetration of a fluid into a porous medium or hele-shaw cell containing a more viscous liquid. *Proceedings of the Royal Society of London. Series A. Mathematical and Physical Sciences* **245** (1242), 312–329, arXiv: <https://royalsocietypublishing.org/doi/pdf/10.1098/rspa.1958.0085>.
- SIGMUNDSSON, FREYSTEINN, PARKS, MICHELLE, GEIRSSON, HALLDÓR, HOOPER, ANDREW, DROUIN, VINCENT, VOGFJÖRD, KRISTÍN S., ÓFEIGSSON, BENEDIKT G., GREINER, SONJA H. M., YANG, YILIN, LANZI, CHIARA, DE PASCALE, GREGORY P., JÓNSDÓTTIR, KRISTÍN, HREINSDÓTTIR, SIGRÚN, TOLPEKIN, VALENTYN, FRIÐRIKSDÓTTIR, HILDUR MARÍA, EINARSSON, PÁLL & BARSOTTI, SARA 2024 Fracturing and tectonic stress drive ultrarapid magma flow into dikes. *Science* **383** (6688), 1228–1235.
- TAN, C. T. & HOMSY, G. M. 1986 Stability of miscible displacements in porous media: Rectilinear flow. *The Physics of Fluids* **29** (11), 3549–3556, arXiv: https://pubs.aip.org/aip/pfl/article-pdf/29/11/3549/12502343/3549.1_online.pdf.
- TAN, C. T. & HOMSY, G. M. 1988 Simulation of nonlinear viscous fingering in miscible displacement. *The Physics of Fluids* **31** (6), 1330–1338, arXiv: https://pubs.aip.org/aip/pfl/article-pdf/31/6/1330/12613351/1330.1_online.pdf.
- TAYLOR, GEOFFREY INGRAM 1953 Dispersion of soluble matter in solvent flowing slowly through a tube. *Proceedings of the Royal Society of London. Series A. Mathematical and Physical Sciences* **219** (1137), 186–203, arXiv: <https://royalsocietypublishing.org/doi/pdf/10.1098/rspa.1953.0139>.
- WHITEHEAD, J. A. & HELFRICH, KARL R. 1991 Instability of flow with temperature-dependent viscosity: A model of magma dynamics. *Journal of Geophysical Research: Solid Earth* **96** (B3), 4145–4155, arXiv: <https://agupubs.onlinelibrary.wiley.com/doi/pdf/10.1029/90JB02342>.
- WYLIE, JONATHAN J., HELFRICH, KARL R., DADE, BRIAN, LISTER, JOHN R. & SALZIG, JOHN F. 1999 Flow localization in fissure eruptions. *Bulletin of Volcanology* **60** (6), 432–440.
- WYLIE, JONATHAN J. & LISTER, JOHN R. 1995 The effects of temperature-dependent viscosity on flow in a cooled channel with application to basaltic fissure eruptions. *Journal of Fluid Mechanics* **305**, 239–261.
- YANG, ULRIKE MEIER & OTHERS 2002 Boomerang: A parallel algebraic multigrid solver and preconditioner. *Applied Numerical Mathematics* **41** (1), 155–177.
- ZIMMERMAN, WB & HOMSY, GM 1991 Nonlinear viscous fingering in miscible displacement with anisotropic dispersion. *Physics of Fluids A: Fluid Dynamics* **3** (8), 1859–1872.
- ZIMMERMAN, W. B. & HOMSY, G. M. 1992 Viscous fingering in miscible displacements: Unification of effects of viscosity contrast, anisotropic dispersion, and velocity dependence of dispersion on nonlinear finger propagation. *Physics of Fluids A: Fluid Dynamics* **4** (11), 2348–2359, arXiv: https://pubs.aip.org/aip/pof/article-pdf/4/11/2348/12673185/2348.1_online.pdf.